Coastal Engineering 157 (2020) 103623

Contents lists available at ScienceDirect

Coastal Engineering

journal homepage: http://www.elsevier.com/locate/coastaleng

Debris-flow generated tsunamis and their dependence on debris-flow dynamics

S.I. de Lange [a], N. Santa [a], S.P. Pudasaini [b], M.G. Kleinhans [a], T. de Haas [a,*]

[a] Faculty of Geosciences, Utrecht University, Utrecht, the Netherlands
[b] Institute of Geosciences, Geophysics Section, University of Bonn, Bonn, Germany

ARTICLE INFO

Keywords:
Landslide
Debris-flow generated tsunami
Wave amplitude
Wave celerity
Physical modelling

ABSTRACT

Debris-flow generated tsunamis can be extremely dangerous for lakeside settlements and infrastructure. Debris-flow composition strongly affects debris-flow thickness and velocity, and therefore also the generated tsunami. This interaction is, however, poorly understood. We investigate the effects of debris-flow volume, composition (gravel, sand, clay, water) and subaerial outflow slope on wave celerity and amplitude in a small-scale physical model consisting of an inclined outflow channel which transits into a three-dimensional water reservoir.

We find that upon debouching, a debris flow pushes the water forward until wave celerity exceeds subaqueous debris-flow velocity (i.e. Froude number <1). The wave then detaches from the debris flow and travels into the far-field. Pushing of the debris-flow oversteepens and accelerates the generated wave beyond the celerity predicted by linear wave theory for shallow waves. It also increases its non-linearity but does not result in wave breaking.

Wave celerity has the strongest relation with debris-flow velocity. Debris-flow velocity increases with increasing water and clay content (up to 22%), which both lubricate the flow. Far-field leading wave amplitude has the strongest relation with debris-flow momentum (velocity times effective mass), which is mostly a function of debris-flow thickness, water and clay content.

We test the applicability of published (semi-empirical) equations for predicting tsunami amplitude generated by dry landslides, and show that they are to some extent also applicable to debris flow. Potential scale effects, especially considering the smallest waves and water depths, could influence the applicability of these predictors and translation of the results to the field scale. Our results demonstrate the importance of debris-flow composition on tsunami generation and evolution, and thus the necessity of including flow composition in predictive simulation models.

1. Introduction

When landslides debouch into standing bodies of water, catastrophic tsunamis, also called impulse waves, can be generated (Atwater and Moore, 1992; Hermanns et al., 2004; Bussmann and Anselmetti, 2010). Tsunamis are long water waves generated by an abrupt disturbance of the bed or surface of a water body (e.g. Kafle et al., 2016). Tsunamis created by landslides are particularly dangerous because of their unpredictability and extreme wave run-up heights (Pudasaini, 2014; Pudasaini and Mergili, 2019). Recent examples of landslide-tsunami hazards stem from for example the Three Gorges Reservoir in China in 2003, where 30 m high waves caused 24 fatalities (Wang et al., 2004), southern Alaska where a wave with an estimated crest amplitude of 100 m and 193 m run-up occurred in 2015 (Higman et al., 2018), and Indonesia where two landslides in September and December 2018 caused ~10 m high waves (Heidarzadeh et al., 2019) and more than 1 000 fatalities.

Key landslide characteristics for tsunami generation, such as slide impact velocity and slide thickness, depend mostly on landslide volume, composition (e.g., grain-size distribution and water content), and slope angle and geometry (Ataie-Ashtiani and Nik-Khah, 2008; McFall and Fritz, 2016; McFall et al., 2018). A wave is generated at the moment the landslide debouches into the water (the impact zone), transferring its momentum to the water body. As the slide penetrates the water, it deforms and flow separation (water body detachment) occurs if the impact velocity is high enough (Fritz et al., 2003a, 2003b). During the impact of

* Corresponding author. Vening Meineszgebouw A, Princetonlaan 8a, 3584 CB, Utrecht, the Netherlands
E-mail address: t.dehaas@uu.nl (T. de Haas).

https://doi.org/10.1016/j.coastaleng.2019.103623
Received 9 July 2019; Received in revised form 6 December 2019; Accepted 21 December 2019
Available online 26 December 2019

the landslide into the water body, an impact crater is created which becomes the leading wave trough (McFall and Fritz, 2016). The initially displaced water becomes the leading wave crest, moving radially away from the impact zone to the near-field. The leading wave is released (detached; Miller et al., 2017) when the wave celerity exceeds the decreasing subaqueous landslide velocity, and subsequently travels into (in generally increasingly deeper water) the far-field (McFall et al., 2018). Ultimately, when the wave approaches the shore or another obstruction, the wave shoals and run-up or overtopping occurs (Kafle et al., 2019). Secondary waves are formed if the impact crater collapses (Fritz et al., 2003b), which happens if the momentum transfer of the debris flow to the water is not large enough to oppose the hydraulic pressure gradient in the upstream direction (Pudasaini, 2014). The characteristics of the tsunamis, such as amplitude and celerity, are a function of both the water body geometry (e.g. depth, volume), and the landslide characteristics (e.g. velocity, thickness) (Huber, 1980; Heller et al., 2009; Heller and Hager, 2011).

Passive methods to mitigate fatalities and damage from tsunamis, such as evacuation or water level lowering of hydropower reservoirs, or active methods such as blasting sites of potential slope failure, require detailed knowledge about the waves that would be generated by a given landslide. For hazard prevention, especially wave celerity and amplitude are of main importance, because these determine the time of arrival and the flooded area, respectively. However, at present we lack the means to accurately predict wave celerity and amplitude because of the complicated landslide-tsunami interactions. Studying landslide-generated tsunamis in nature is complicated due to their unpredictable occurrence in space and time. Physical experiments overcome this problem and have the additional advantage that initial and boundary conditions can be fully controlled. Detailed measurements of both the landslide and waves can be made in experiments, which is hardly possible in the field (Paola et al., 2009; Van Rijn et al., 2011; Kleinhans et al., 2014). Furthermore, carefully documented results from landslide-generated tsunami experiments might be used to verify and calibrate numerical models (Quecedo et al., 2004; Zweifel et al., 2007; Pudasaini, 2012, 2014; Ma et al., 2015; Kafle et al., 2016, 2019).

Previous experimental studies (Table 1) of landslide generated tsunamis have been conducted on various scales, and include simplified two- and three dimensional (2D and 3D) experiments with the landslide represented by non-deformable blocks (e.g. Noda, 1970; Panizzo et al., 2005; Najafi-Jilani and Ataie-Ashtiani, 2008; Saelevik et al., 2009; Heller and Spinneken, 2015) or granular uniform sized sediment (e.g. Fritz et al., 2004; Heller and Hager, 2010; Heller and Hager, 2011; Mohammed and Fritz, 2012; McFall and Fritz, 2016, McFall et al., 2018). Important recent contributions that result from these experimental investigations include characterization of near-field wave features (Fritz et al., 2004), the prediction of wave shape by a semi-empirical equation (Heller and Hager, 2011) and estimations of wave amplitude with semi-empirical (Fritz et al., 2004; Heller and Hager, 2010) or momentum-based equations (Mulligan and Take, 2017; Bullard et al., 2019). Recently developed equations for predicting wave amplitude have been tested by Miller et al. (2017), and were improved by implementing effective instead of total debris-flow mass.

A lot of progress in understanding landslide generated tsunamis has thus been made with these experimental studies. Nevertheless, these studies were often performed in a 2D rather than 3D setting (Fritz et al., 2004; Heller and Hager, 2010, 2011; Miller et al., 2017; Bullard et al., 2019), and landslides generally consisted of single-size grains only without water (Fritz et al., 2004; Mohammed and Fritz, 2012; McFall and Fritz, 2016). In nature landslides often contain an interstitial fluid which enhances the landslides mobility (Legros, 2002; Pudasaini and Miller, 2013; Pudasaini and Mergili, 2019), although existing experiments do not consider these aspects. Only the recent study of Bullard et al. (2019) studies highly mobile water-saturated landslides, and acknowledges the influence of water on the landslide behavior. These simplifications affect both the landslide and wave characteristics, as well as their interaction. Studies have shown that 2D experiments overestimate the wave amplitude significantly (Mohammed and Fritz, 2012; Heller and Spinneken, 2015; McFall and Fritz, 2016). Moreover, the composition of a landslide strongly controls its slide thickness, slide velocity and slide density (de Haas et al., 2018), which on their turn affect the generated wave (Ilstad et al., 2004; McFall and Fritz, 2016; Yin and Rui, 2018). The subaerial debris-flow study of de Haas et al. (2015) showed a significant influence of debris-flow composition on runout length (the maximum length of the landslide deposit). Subaqueous landslide studies found that water and clay content strongly influence coherence of the slide (Yin and Rui, 2018), the pore pressure and the bed friction (Ilstad et al., 2004). Finally, McFall and Fritz (2016) found that cobble landslides produce higher wave amplitudes than gravel landslides, due to more efficient energy transfer caused by the high momentum of the cobble landslides.

To improve our understanding of landslide-generated tsunamis, we thus need dedicated experiments wherein the effects of landslide composition (including water and granular material) on wave

Table 1
Summary of the methods used in various comparable studies.

Reference	This study	Fritz et al. (2004); Heller and Hager (2010); Heller and Hager (2011);	Mohammed and Fritz (2012)	Heller and Spinneken (2015)	McFall and Fritz (2016)	Mulligan and Take (2017); Miller et al. (2017);	Bullard et al. (2019)
Type of landslide	granular, varying grain size, saturated	granular, constant grain size, forced velocity and thickness	granular, non-uniform grain size, forced velocity and thickness	rigid PVC-slides, forced velocity and width	granular, 2 sediment types	granular, constant grain size	granular, water-saturated
2-dimensional (2D) or 3-dimensional (3D)	3D	2D	3D	2D, 3D	3D	2D	2D
Scale outflow slope	2.0 × 0.1 m 20–40°	3.0 × 0.5 m 45°	9.3 × 1.2 m 27°	21.0 × 0.6 m 45°	9.3 × 1.2 m 27°	6.7 × 2.1 m 30°	6.7 × 2.1 m 30°
Scale wave basin	1.9 × 0.9 m with sloping bed (10°)	11.0 x 0.5 × 1.0 m	48.8 × 26.5 m	20.0 × 7.4 m	48.8 × 26.5 m	33.0 × 2.1 m	33.8 × 2.1 m
Water depth	0–0.33 m (sloping)	0.30, 0.45, 0.68 m	0.30, 0.60, 0.90, 1.20 m	0.24, 0.48 m	0.30, 0.60, 0.90, 1.20 m	0.05–0.50 m	0.15–0.65 m
Parameter variations	debris-flow volume, debris-flow composition, outflow slope	landslide velocity, landslide thickness, water depth	landslide volume, landslide velocity, water depth	landslide velocity, water depth	landslide volume, sediment type, shape of outflow slope, water depth	landslide volume, water depth, water content debris-flow	landslide volume, water depth

characteristics are systematically explored. In this study we investigate tsunami generation by debris flows. Debris flows are a subtype of landslides that consist of dense masses of water, soil and rock that can flow down slopes at high velocities (e.g., Johnson, 1970; Iverson, 1997), and which are known to be capable of generating tsunamis (Watts and Walder, 2003; Walder et al., 2006; Dawson and Stewart, 2007). Recently, there has been many progress on creating small-scale debris flows on the laboratory scale (e.g. D'Agostino et al., 2010; Scheidl et al., 2014; Hürlimann et al., 2015; de Haas et al., 2015, 2016; 2018; de Haas and van Woerkom, 2016), and the effects of debris-flow composition on debris-flow dynamics have been experimentally explored (e.g., de Haas et al., 2015). These experimental advances open up the possibility of generating tsunamis by more nature-like small-scale debris flows, consisting of a dense mixture of sediment and water, and to study effects of changes in the debris-flow composition on wave characteristics.

Here, we perform a series of small-scale debris-flow-tsunami induced experiments in a 2D-3D setting. Our main objective is to unravel the influence of debris-flow volume, debris-flow composition and subaerial slope on tsunami characteristics. Secondly, we intend to find suitable predictors for tsunami celerity and amplitude. In our study we maximize variability by including debris flows of widely varying volume and composition, defined by their water, clay and coarse-particle content. This is in contrast with previous experimental investigations on landslide-tsunami interactions wherein dry landslides generally consisted of a uniform or a simplified (non-varying) composition (e.g., Fritz et al., 2004; Mohammed and Fritz, 2012; Heller and Hager, 2010, 2011; McFall and Fritz, 2016). Finally, the data obtained from the experiments are important to calibrate and validate the multi-phase particle-fluid mixture debris flow models (e.g. Pudasaini and Mergili, 2019), and simulation tools such as r.avaflow (Mergili et al., 2017, 2018a,b).

This study provides observations necessary for understanding tsunami generation and evolution by debris flows. After we detail the methods (section 2), we give a general description of the observed phenomena (section 3.1), discuss the debris-flow and wave characteristics (sections 3.2) and test relations between debris-flow properties and the resulting tsunami (section 3.3). In the discussion the laboratory results are interpreted and compared to previous research (section 4.1), and we assess the applicability of predictors for wave celerity and leading wave amplitude, and previously determined predictive equations for maximum wave amplitude, to debris flows (section 4.2). In section 4.3 we consider the downscaling of natural processes into an experimental setup and finally, we list the main findings of the research (section 5).

2. Methods

2.1. Methodology

To study the influence of debris-flow volume and composition and channel slope on wave generation and evolution, a series of 60 small-scale experiments was conducted (Tables 2 and S1 in supporting information). To do so, we extended the debris-flow flume of de Haas et al. (2015), which was originally used to study subaerial debris-flow dynamics and deposits, with a water basin into which the experimentally generated debris flows could debouch and tsunamis could form. Our small scale experimental approach allowed many systematic experiments to be performed in a relatively short amount of time. Below we describe the experimental setup, debris-flow composition, and the methods used to analyze the data.

2.2. Experimental setup

The experimental setup consisted of three sections (Fig. 1): (1) a tank to stir the sediment-water mixture, (2) a 2 m long and 12 cm wide

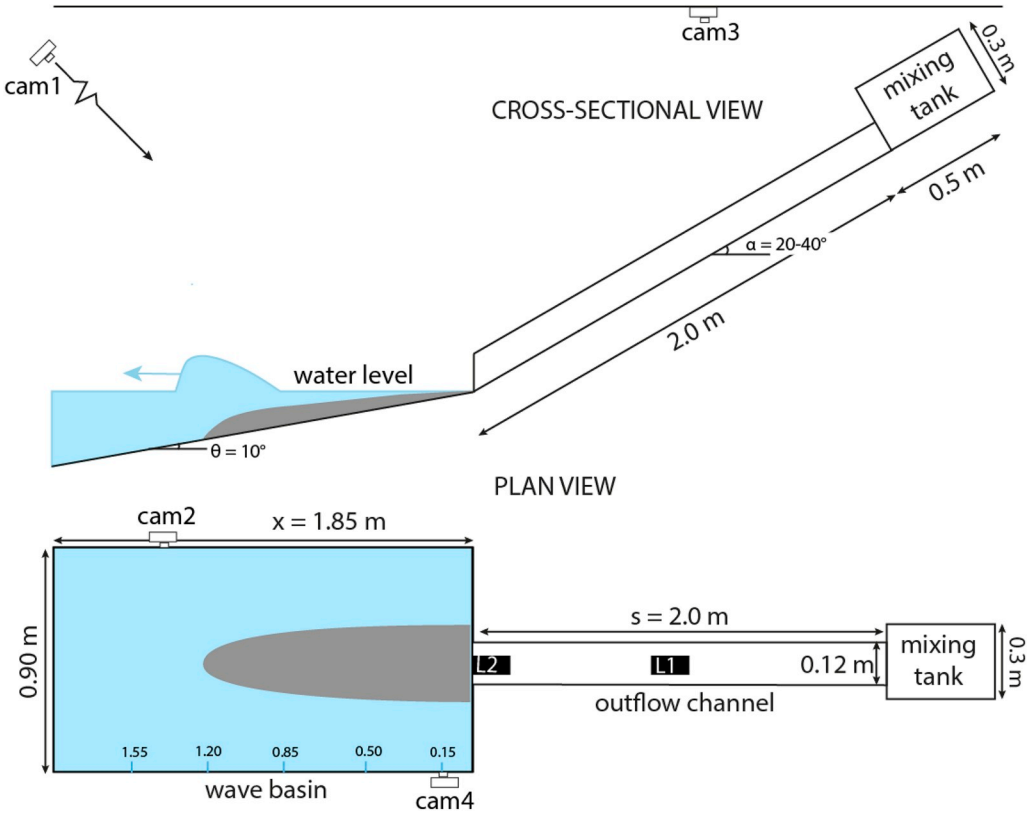

Fig. 1. Overview of the experimental setup. The debris flow is released from mixing tank and flows via the outflow channel into the wave basin, where it causes tsunamis to develop. Water level is measured at a distance of 0.15, 0.50, 0.85, 1.20 and 1.55 m from channel outlet with imagery from cam2. Cam = camera. L = laser. Extended from de Haas et al. (2015).

subaerial outflow channel, inclined at 20–40° depending on the experimental conditions, and (3) a 0.90 m wide and 1.85 m long wave basin with a floor inclined at 10°. The outflow channel had a rectangular geometry, and was covered with sand paper to create surface roughness. Sediments were manually mixed for approximately 20 s in the tank for each experiment and then released electromagnetically through an upwards swinging hatch.

The substantially greater width of the wave basin compared to the subaerial outflow channel allowed for 3D wave propagation, while its fixed rough surface, created by gluing sand (coarse sand in Fig. 2) to the bottom plate, provided basal friction. In all experiments the water level of the wave basin exactly matched the base of the outflow channel. The water depth linearly increased with distance from the base of the outflow channel as a result of the 10° basin-floor inclination. In the near-field (x = ~0–0.85 m) the water depth increases from 0 to ~0.15 m, in the far-field (x > ~0.85–2 m) a maximum depth of 0.33 m at the far end of the reservoir is reached. The total water volume of the wave basin was 0.275 m^3.

Multiple cameras recorded debris-flow and wave dynamics (Fig. 3A and B). GoPro HERO6 cameras were used (1) to capture a general overview of the experiment (cam1), (2) to extract wave celerity and amplitude from the side of the water basin (cam2, distance from channel outlet x = 1.30 m), and (3) to extract the debris-flow velocity in the subaerial outflow channel (cam3, distance from mixing tank s = 1.20 m). The resolution of these cameras was set to 1440ppi with a frame rate of 60fps. A GoPro HERO4 was used to record the impact zone and the near-field wave generation (cam4, at distance from channel outlet x = 0.05 m). This camera had a resolution of 1080ppi and a frame rate of 48fps.

The wave profile (wave height over time) was extracted at 5 different locations along the side of the wave basin, at a distance of 0.15, 0.5, 0.85, 1.20, and 1.55 m from the channel outlet. This introduces the uncertainty that wave amplitude was at its maximum in between these discrete locations, hence the actual maximum wave amplitude might deviate slightly from the values recorded in this study. The water in the basin was colored with blue dye to enhance the visibility of the water level in video imagery, which assured easy observation of the exact location of the water level. Based on color differences between below water (dyed with brilliant blue) and above water (white), water level was extracted automatically from the video imagery (Fig. 3C). Wave height was extracted with an accuracy of ~1.5 mm, corresponding to the pixel size of the GoPro imagery. We only considered the first 2 s after the onset of wave formation at a specific location, because of wave reflection and refraction beyond that time. To limit effects of reflection, we perform most of our analyses based on the leading wave. In section 4.2 the maximum wave amplitude becomes important, fortunately the time frame of 2 s is enough to detect 92% of the maximum wave heights (occurring within the first three waves). The amplification of wave amplitude due to run-up on the longitudinal vertical walls of the wave basin, is largely negligible due to the incipient wave angle and the smoothness of the wall.

Two lasers, L1 (Baumer OADM 20U2480/S14C) and L2 (Baumer FADK14U4470/S14/IO), were used to measure the flow thickness near the middle (distance from mixing tank s = 1.20 m) and the end (x = 1.90 m) of the subaerial outflow channel. Debris-flow weight was measured with a circular load cell (radius 1.6 cm) in the middle of the outflow channel (at distance of s = 1.20 m from mixing tank) and recorded with a frequency of 100 Hz.

2.3. Debris-flow composition

The experimental debris flows consisted of four different types of sediment: clay (kaolinite), well sorted fine sand, poorly sorted coarse sand, and basaltic gravel (2–5 mm). Similar sediment was previously used to create experimental debris flows by de Haas et al. (2015, 2016; 2018) and de Haas and van Woerkom (2016). The sediment sizes were chosen so that the clay increased the viscosity of the flow, while the gravel could accumulate at the front of the flow, both mimicking natural debris-flow behavior (de Haas et al., 2015). The reference mixture of 8.0 kg (0.0041 m^3) consisted of 18.00 vol% gravel, 59.00 vol% coarse sand, 21.00 vol% fine sand, 2.00 vol% clay and 0.44 vol% water, (Table 2). The volume percentages of particles refer to the volume ratio of solid particles, while the volume percentage of water refers to the volume ratio of both the solid and liquid phase. Mass was converted to volume by assuming a constant grain density of 2 650 kg/m^3 for coarse sand, fine sand and clay, 3400 kg/m^3 for basaltic gravel and 1 000 kg/m^3 for water. Effects of flow volume, composition, and subaerial outflow slope were explored by systematically varying these parameters around the reference flow (Tables 2 and S1). To quantify the natural variability within the flows and its influence on the obtained trends, all experiments were performed at least in twofold.

2.4. Data analyses

Wave celerity c was estimated from the difference in arrival time between the first crest and trough at the five wave measurement locations at the side of the water basin (Fig. 3 and Fig. S1 in supporting information). Wavelength λ was defined by the distance between two consecutive waves, which we calculated by multiplying the wave celerity with the wave period T (λ [m] = c [m/s] * T [s]). The breaking criterion (crest amplitude (a_c [m])/still water level (h [m]) = 0.78; McCowan, 1894) was used to determine if waves could theoretically

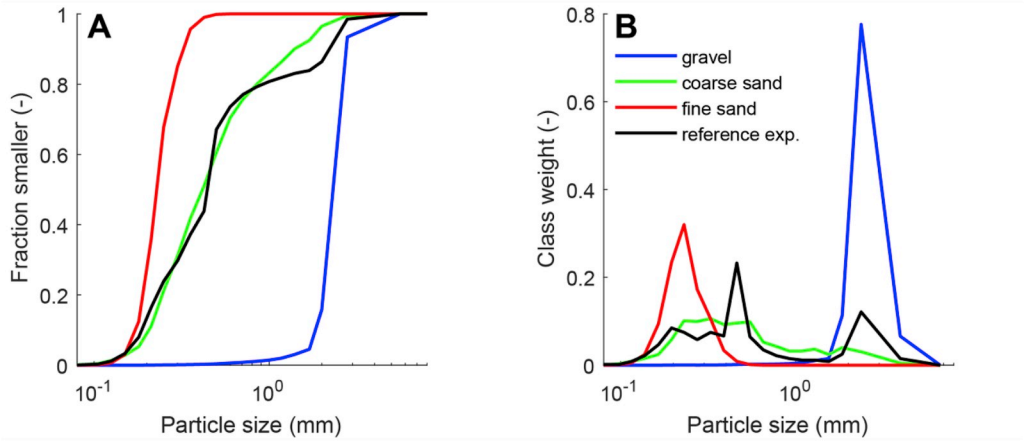

Fig. 2. A) Cumulative particle distribution of the four sediment types (clay excluded) and the reference mixture. B) Frequency distribution of the sediment types. Figure modified from de Haas et al. (2015).

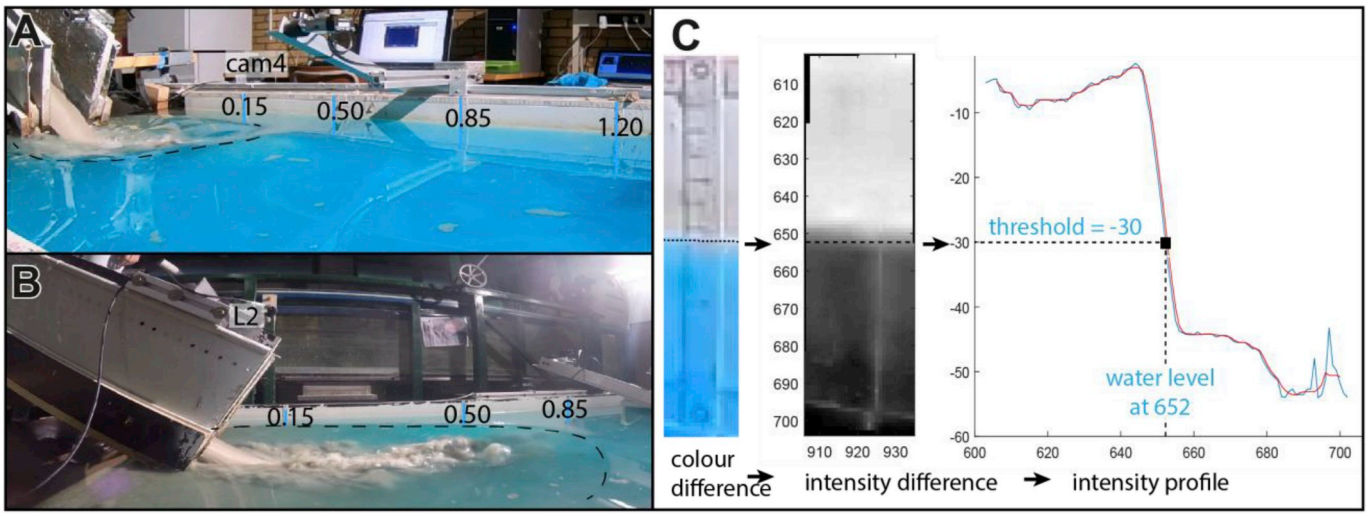

Fig. 3. Wave generation with cam2 (A) and cam4 (B). The distance from channel outlet 0.15, 0.50, 0.85 and 1.20 m refer to the measurement locations where water level over time is extracted, the dashed line is the wave front of the leading wave. L2 = laser to measure debris-flow thickness at the outlet of the outflow channel. C) Example of automatic extraction of water level out of camera footage of cam2 (at a distance from the channel outlet x = 0.85 m). The color difference between the blue water and white background is used to calculate color intensity values. A threshold value (of in this case −30) is used to distinguish between water and no-water. (For interpretation of the references to color in this figure legend, the reader is referred to the Web version of this article.)

Table 2
Overview of conducted experiments per studied parameter. See Table S1 in supporting information for the parameter variations within the experimental runs.

Parameter	Unit	Reference mixture	Experimental range	Nr. of subaqueous experiments
Debris-flow composition				
Volume (mass)	m^3 (g)	0.0042 (8000)	0.0018–0.0092 (3 500–18 000)	22
Water fraction	g	1846	1 600–2 900	8
	vol %	44	39.9–60.1	
	wt%	23.08	20.0–36.3	
Gravel fraction	g	1107	0–3 921	10
	vol %	18.00	0–63.7	
	wt%	13.85	0–49.0	
Clay fraction	g	123	0–1784	10
	vol %	2.00	0–29.0	
	wt%	1.54	0–22.3	
Topography				
Slope	°	30	20–40	8

break in this setup. The detachment time, or effective time (t_{eff} [s]), was visually defined as the time at which the subaqueous debris flow was no longer connected to the tsunami and stopped pushing the wave (Miller et al., 2017). At this moment, the wave celerity exceeded the debris-flow velocity.

We defined debris-flow momentum (M [kg m/s]) as effective mass (m_{eff} [kg]) times downslope velocity (u_{df} [m/s]).

$$M = m_{eff}\, u_{df} \tag{1}$$

wherein the effective mass (following Miller et al., 2017) was the total amount of mass of the debris flow debouching into the wave basin before wave detachment, and the debris-flow velocity was averaged over the outflow slope:

$$m_{eff} = \int_{t_0}^{t_{eff}} m_{df}\, dt \;(u_{df}\; t_{eff}) \tag{2}$$

where m_{df} [kg/m] denotes the debris-flow mass at the end of the outflow slope, just before impact. It was calculated by taking the measured weight at the middle of the outflow slope ($m_{df} = m_{measured}$ [kg]$/A_{load\ cell}$ [m^2] * *width of flume* [m]) and scaling this with the measured debris-flow thickness in the middle and at the end of the outflow slope, assuming constant debris-flow density: m_{df} * (h_{outlet}/h_{middle}).

Debris flow and wave energy (E_{df} [J] and E_w [J]) were calculated through equations (3) and (4), respectively.

$$E_{df} = \frac{1}{2} m_{eff}\, u_{df}^2 \tag{3}$$

$$E_w = m\, g\, h = {}^1\!/_2\; w\, \rho_w\, g\, c_d \int_0^{\lambda_d} a_{cd}^2\, dt \tag{4}$$

in which w [m] is the width of wave basin, ρ_w [kg/m^3] is the density of water, g [m/s^2] is the gravitational constant, c_d [m/s] is the wave celerity at 0.85 m along the wave basin, λ_d [m] is the wavelength at 0.85 m along the wave basin and a_{cd} [m] is the crest amplitude at 0.85 m along the wave basin.

For the debris flow, kinetic energy was determined at the moment of debouching into the water basin, while for the leading wave crest, energy was determined at approximately the moment of detachment (at ~0.85 m along the wave basin; where the wave energy was generally the largest). The wave energy consisted of potential energy (expressed by the wave amplitude) and kinetic wave energy (the orbital motion). Assuming equipartition of the energy, wave energy was expressed as 2 times the potential wave energy (Lamb, 1932; McFall and Fritz, 2016). It was assumed that the width of the radial wave was approximately similar to 0.5 times the circumference of a perfect circle with a radius of 0.85 m (wherein 0.85 m taken as the detachment length).

2.5. Maximum crest amplitude predictors

Previous studies have developed various approaches to predict maximum crest amplitude (a_c *[m])*, which are mainly based on landslide parameters, such as the landslide Froude number, landslide outflow thickness and mass (Fritz et al., 2004; Heller and Hager, 2010) or on

momentum transfer (Mulligan and Take, 2017). We will assess the suitability of these predictors to our dataset, and investigate their utility for predicting the crest amplitude of a 3D debris-flow generated wave in section 4.2.2.

Fritz et al. (2004) performed 2D granular landslide experiments, in which the material was pneumatically accelerated. They applied multiple regression for the wave crest amplitude, resulting in the following relation with the debris-flow Froude number:

$$\frac{a_c}{h} = 0.25\ \mathrm{Fr}_{\mathrm{MT}}^{1.4}\left(\frac{h_s}{h}\right)^{0.8} \tag{5}$$

wherein h [m] is still water depth and h_s [m] the landslide outflow thickness. The Froude number (Fr [−]) is the impact slide velocity (u_s [m/s]) divided by the wave celerity ($c = \sqrt{ghcos\theta}$ [m/s]) in the still water depth.

$$\mathrm{Fr} = \frac{\mathrm{u_s}}{\sqrt{ghcos\theta}} \tag{6}$$

wherein θ [rad] is the slope of the wave basin (here, $\theta = 10$). The implementation of this equation is not strictly valid with regard to the classical Froude number. The subaqueous debris-flow velocity u_s is not measured in our setup, rather we measured the velocity of the debris flow during outflow and at the time of impacting the reservoir. Hence, the debris-flow velocity is not measured at the same moment and location as the wave celerity c. Instead, the average debris-flow velocity is chosen at the transition from the inclined channel to the outflow slope, which might be an overestimation of the debris-flow velocity.

Mulligan and Take (2017) corrected the Froude number by accounting for slide thickness relative to water depth and bulk density differences between the sliding material and the water (buoyancy, Pudasaini, 2012). This correction factor was also applied to equation (6), providing much better correlations (e.g. $R^2 = 0.42$ instead of 0.21 when applying equation (5) to our dataset, and $R^2 = 0.54$ instead of 0.25 when applying equations (9) and (10)):

$$\mathrm{Fr}_{\mathrm{MT}} = \frac{u_s}{c}\sqrt{\frac{h_s}{h}\frac{\rho_s - \rho_w}{\rho_w}} \tag{7}$$

Implementing the wave celerity predicted by the shallow wave approximation ($c = \sqrt{ghcos\theta}$) in these equations was found to give better correlations in our research than using the measured wave celerity. Note that this celerity predictor was not directly applicable to the data presented here. A large variability in measured celerity, generated by the different types of debris flows, caused wave celerity not to be a simple function of water depth.

In Heller and Hager (2010)'s experiments, they also forced the acceleration of the granular material. They varied water depth, landslide velocities, slide thickness and slope. Their semi-empirical relation is based on the impulse product parameter (P [−]), and both landslide thickness (h_s) and mass (m_s) are taken relative to still water level (h).

$$\mathrm{P} = \mathrm{Fr}_{\mathrm{MT}}\left(\frac{h_s}{h}\right)^{0.5}\left(\frac{m_s}{\rho b h^2}\right)^{0.25}\cos\left(\frac{6\alpha}{7}\right)^{0.5} \tag{8}$$

$$\frac{a_c}{h} = \frac{4}{9}\,\mathrm{P}^{0.8} \tag{9}$$

In which α [rad] is the slope of the outflow channel. This prediction was improved by Miller et al. (2017) by implementing the effective mass (equation (2)) instead of the total mass, to account for the fact that only a portion of the landslide mass forms the leading wave crest. Here we followed Miller et al. (2017) and applied the effective mass approach to our data. The effective mass was made dimensionless as in equation (8), since this results in a more accurate prediction.

$$\mathrm{P} = \mathrm{Fr}_{\mathrm{MT}}\left(\frac{h_s}{h}\right)^{0.5}\mathrm{m}_{\mathrm{eff}}^{0.25}\cos\left(\frac{6\alpha}{7}\right)^{0.5} \tag{10}$$

The prediction of Mulligan and Take (2017) is based on hydrostatic momentum transfer from landslide to water. This resulted in an analytical equation of the near-field maximum wave amplitude in a 2D-wave field, based on landslide properties. The equation was developed for (near) dry granular landslides, with a lower mobility than debris flows. Mulligan and Take (2017) therefore expected that the underlying assumption of momentum transfer is less applicable for debris flows:

$$\mathrm{a_c} = \sqrt{h^2 + \frac{2\rho_s h_s u_s cos\alpha L_e}{\rho g t_{eff}}} - \mathrm{h} \tag{11}$$

To apply this equation to our research, an estimation of the length scale (L_e [m]) was required.

$$\mathrm{L_e} = 0.5\ \mathrm{u_s}\cos\alpha\ \mathrm{t_{eff}} \tag{12}$$

The length scale was defined as the horizontal distance the landslide travels until detachment, the detachment length, which we predicted following Mulligan and Take (2017), assuming a constant deceleration from impact to deposition over the detachment time. Here, $u_s\cos(\alpha)$ appears due to the projection of u_s along the horizontal direction. The projection of the velocity is used to compare the results with Mulligan and Take (2017).

Implementing this in equation (11) gives:

$$\mathrm{a_c} = \sqrt{h^2 + \frac{\rho_s h_s (u_s cos\alpha)^2}{\rho g}} - \mathrm{h} \tag{13}$$

Bullard et al. (2019) adjusted this equation to make it suitable for highly mobile water-saturated landslides. They increased the effective length L_e with a factor 2 so that the full landslide impact velocity generates the wave. Implementing this in equation (11) gives:

$$\mathrm{a_c} = \sqrt{h^2 + \frac{2\rho_s h_s (u_s cos\alpha)^2}{\rho g}} - \mathrm{h} \tag{14}$$

3. Results

In this section we first describe the general observations made during the experiments. Hereafter we discuss the influence of the variations in debris-flow volume, composition and outflow slope on the debris-flow dynamics and the resulting tsunamis. Finally, we try to identify the effects of all different debris-flow types on the resulting waves.

3.1. General observations

3.1.1. Natural variability

Natural variability and repeatability were evaluated by plotting several debris-flow and wave parameters of two experiments with similar initial and boundary conditions against each other and studying their correlation (Fig. 4). The debris-flow characteristics and wave parameter values showed a significant amount of variability (indicated by the R^2-value), although >98% of the data points fell within the 1:2 lines. Parameters averaged over distance (e.g. average debris-flow velocity or average crest or trough celerity) showed in general less variability than single point measurements. Besides debris-flow thickness at the outlet, near field wave amplitude showed the most variability.

3.1.2. Debris flow dynamics

The mean frontal debris-flow velocity through the subaerial channel was on average 2.12 m/s with standard deviation of 0.32 m/s, and no significant acceleration due to outflow was measured. Flow thickness was largest near the front of the flow (Fig. 5). The thickness of the debris

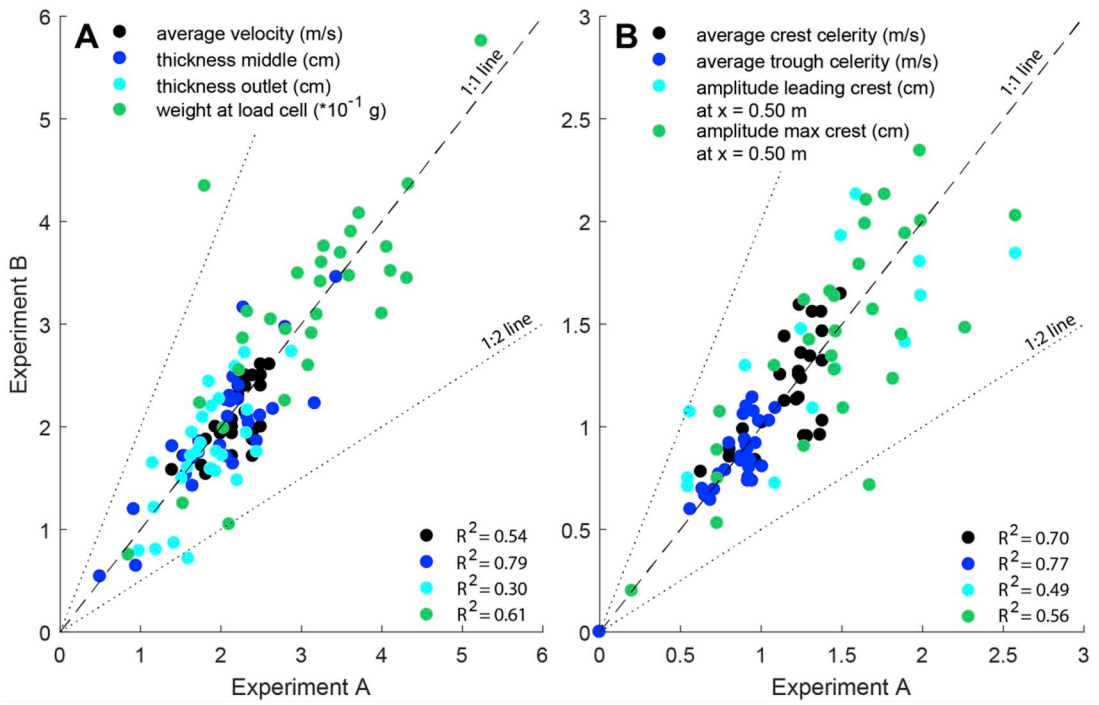

Fig. 4. Natural variability of A) debris flows and B) the corresponding waves. The numbers on the axis correspond with the actual values of the plotted variables. Experiment A and B on the x- and y-axis denote two experiments with similar initial and boundary conditions.

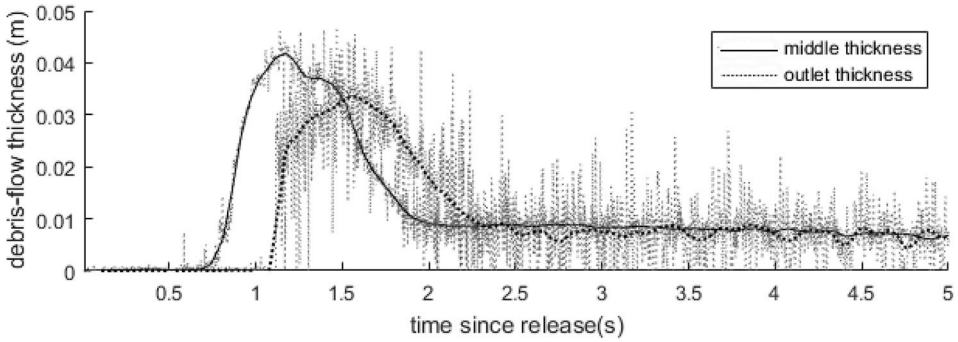

Fig. 5. Example of a hydrograph of debris-flow thickness (exp. 022, V = 9.17 dm^3), measured with two lasers in the middle and at the outlet of the outflow channel. Data were smoothened with a moving average of 0.1 s. The grey lines indicate the original signal.

flow was generally larger in the middle than at the outlet (2.04 cm and 1.81 cm, respectively), presumably due to the time needed for the debris flow to spread out.

As the debris flow hits the water, fines (clay) partly escaped the debris-flow mixture and were suspended into the water column, while the larger grains continued flowing over the basin floor. The debris flow displaced the water and transferred its momentum. Ultimately, it slowed down, stopped and formed a deposit on the basin floor.

3.1.3. Tsunami generation and evolution

The debris flow pushed the water forward, until the wave celerity exceeded the subaqueous debris-flow velocity and the wave was detached (Fig. 6). The waves travelled away radially from the point source where the debris flow entered the water basin, its radial shape being independent of the debris-flow characteristics. The leading wave oversteepened and accelerated by the pushing of the debris flow (Fig. 7) and its crest amplitude was typically at its maximum just after detachment (generally around a distance of 0.50–0.85 m from channel outlet, where the water depth is 0.08–0.15 m; Fig. 8). When the wave travelled out of the near-field region (x < ~0.85 m) into the far-field region (x > ~0.85 m), the wave celerity decreased and slowly returned to its value predicted by linear wave theory. The period of the waves increased while travelling and the wave gradually flattened out.

The amplitude of the maximum crest always matched or exceeded the maximum trough amplitude, however, when looking at the leading crest and trough amplitudes, this was not the case. A relatively deep wave trough followed the leading crest (Fig. 8) with its amplitude on average similar to the amplitude of the leading crest, but which could be up to 3 times larger in the impact zone. In the near-field, the leading trough amplitude exceeded the leading crest amplitude in 73% of the experiments. This percentage decreased to 70, 45 and 20% at 0.85, 1.20 and 1.55 m along the wave basin, from which follows that in the far-field, the crest amplitude was larger than the through amplitude. The trough celerity was on average 1.4 times lower than the crest celerity.

The leading wave amplitude was also the maximum wave amplitude for 28% of the time in all five locations. At location x = 0.50 m, the wave with the maximum amplitude at that location was most frequently the leading wave (68%), while after detachment this number reduced to ~20%. Here, the maximum crest was most often the second or third wave. The maximum crest amplitude was on average 1.33 times larger

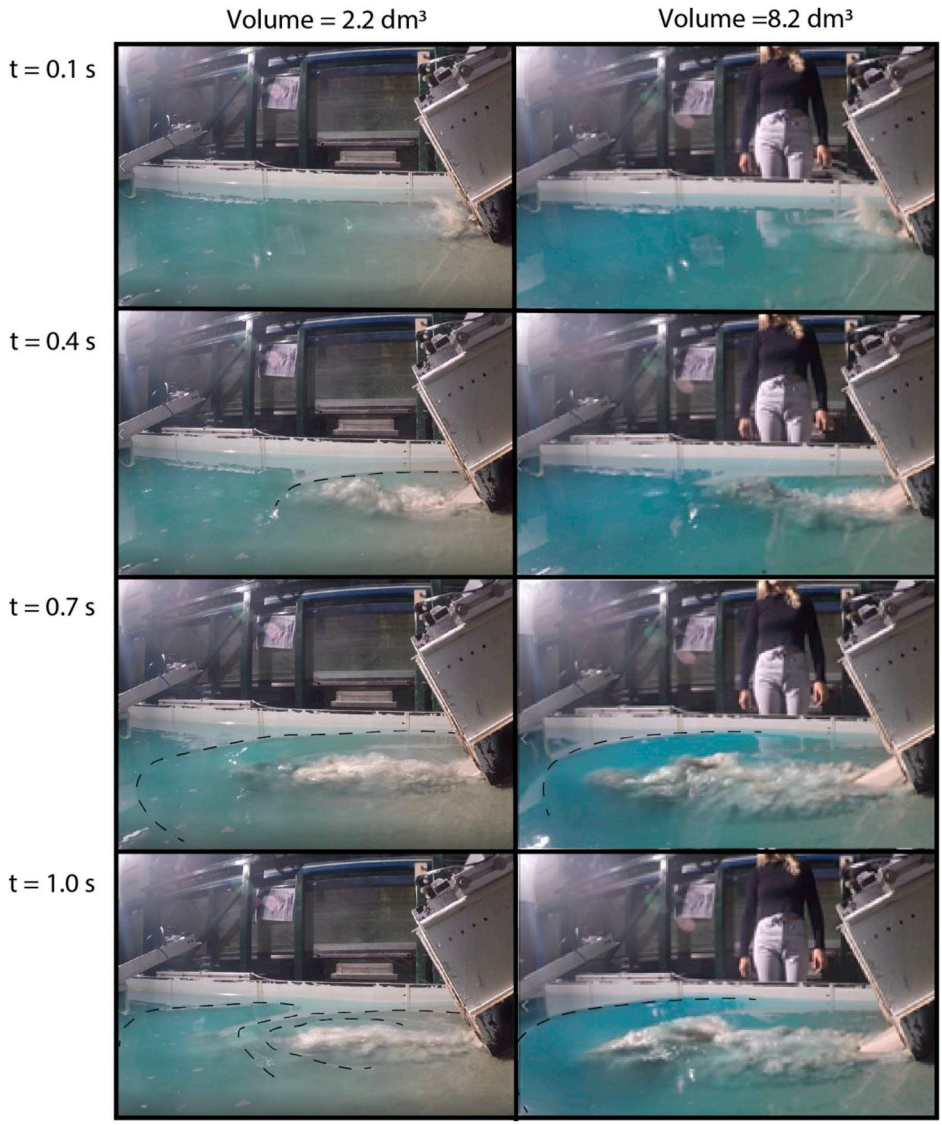

Fig. 6. Wave generation and propagation in the first second after impact, for a small and large debris-flow volume. Detachment can be seen for V = 2.2 dm^3 at >0.4 s and for V = 8.2 dm^3 at 0.7 s.

than the leading crest amplitude. There was no relation between debris-flow characteristics and ratio between leading and maximum crest amplitude.

All experiments took place in the intermediate water regime ($0.05 < h/\lambda < 0.5$) and no breaking occurred. All waves were highly non-linear (based on equation (S12) in supporting Table S4), with their linearity increasing with increasing distance from the impact zone.

3.2. *Effects of debris-flow volume, composition and topography on tsunami generation and evolution*

3.2.1. *Initial flow volume*

Debris-flow velocity increases with increasing flow volume, but this relation shows a lot of variability ($R^2 = 0.44$). The fixed width of the channel slope causes debris-flow thickness to increase with increasing volume ($R^2 = 0.88$) (Fig. 9 A, B). Upon entering the water basin, the flows with a low volume show a relatively small amount of air entrainment, a quick release of the wave and therefore the development of more, smaller waves following the leading crest (Fig. 10 A, B and movie S1 in the supporting information). Very low debris-flow volumes cause waves with such a low crest amplitude (<2 mm) that surface tension may start to play a role and scale effects become more important (section 4.3). An increasing volume leads to the development of a forwards collapsing impact crater and even more turbulence in the wave basin. Large grains (basaltic gravel) jump out of the water or follow the turbulent upper layer of the water (movie S2 in supporting information). As the debris-flow volume increases, the wave crest and trough amplitude (both leading and maximum) and the wave celerity increase as well (Fig. 10 A, B).

Supplementary data related to this article can be found at https://doi.org/10.1016/j.coastaleng.2019.103623.

3.2.2. *Debris-flow composition*

With an increasing water content, the average velocity of the debris flow increases ($R^2 = 0.90$). The maximum thickness also increases with water content ($R^2 = 0.56$), due to the larger increase in frontal velocity compared to body velocity, promoting the accumulation of material at the front of the flow (Fig. 9 C, D). The wave evolution caused by debris flows with a low water content is characterized by a quick dispersion of waves (movie S3 in supporting information). When increasing the water content, a forward collapsing impact crater is visible, the wave develops a steeper front, and the detachment time increases (movie S4 in supporting information). An increase in water content results in an increase in debris-flow velocity and thickness, and as a result a higher and faster

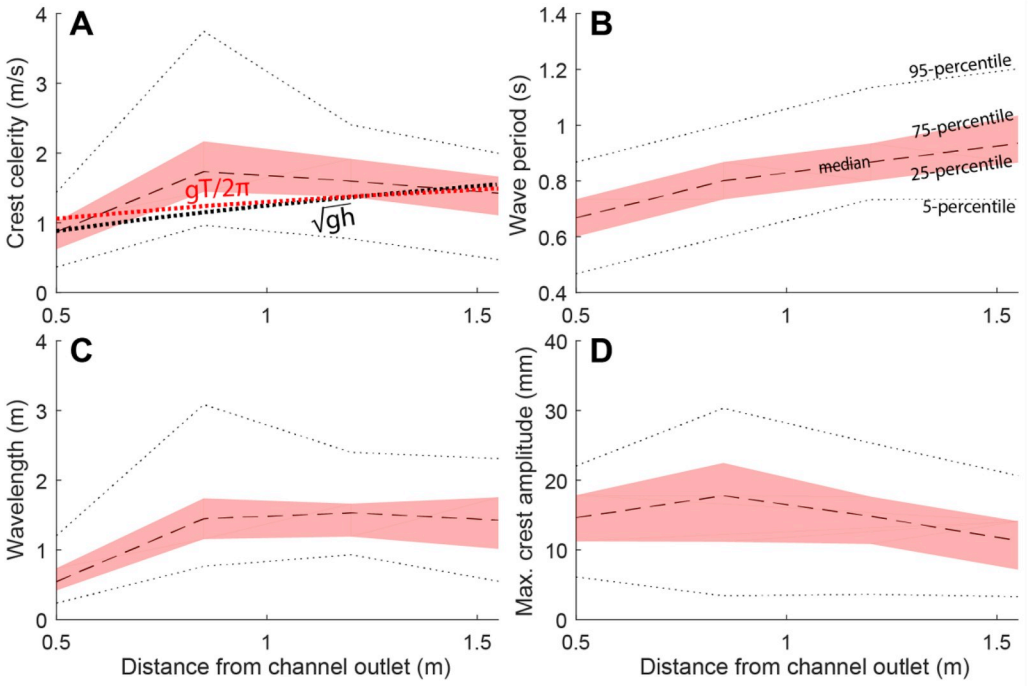

Fig. 7. Development of wave characteristics over distance from the channel outlet. The median value of all experimental runs at these locations is indicated with a dotted line, the shaded area indicates the 25 and 75 percentile, the thin lines the 5 and 95 percentile. A) crest celerity. The red dotted line is the predicted value according to the deep water equation ($c = gT/2\pi$), the black dotted line is the shallow water equation ($c = \sqrt{gh}cos\theta$) B) wave period C) wavelength D) maximum wave crest amplitude. (For interpretation of the references to color in this figure legend, the reader is referred to the Web version of this article.)

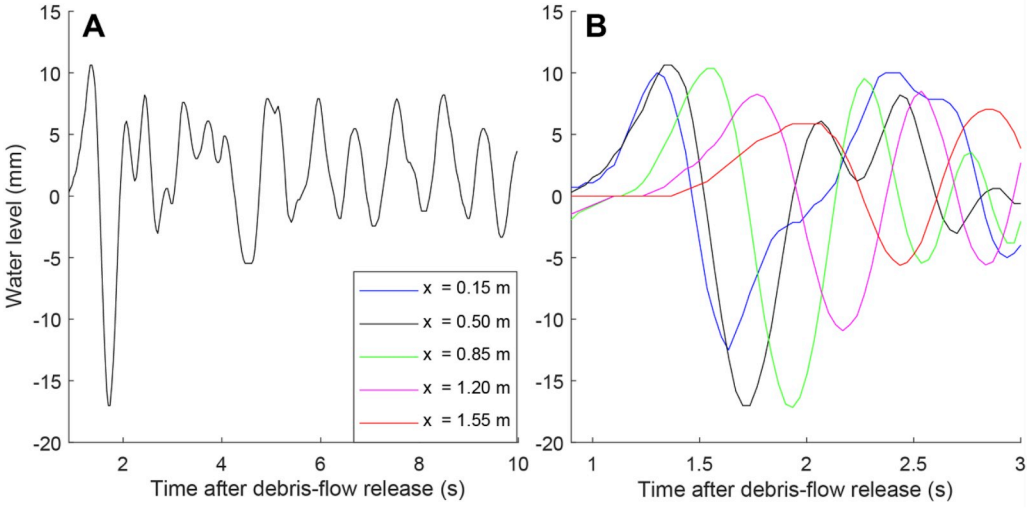

Fig. 8. Wave profile for reference experiment 010, smoothened with moving average over 0.1 s. A) Wave profile at 0.50 m from channel outlet over the first 10 s after debris flow release. B) Leading crest and trough at 0.15, 0.50, 0.85, 1.20 and 1.55 m from channel outlet.

moving wave. Especially the relation between water content and wave celerity is strong ($R^2 = 0.91$), in contrast to the relation with wave amplitude (Fig. 10 C, D).

Supplementary data related to this article can be found at https://doi.org/10.1016/j.coastaleng.2019.103623.

An increase in clay content has a lubricating effect resulting in a larger debris-flow velocity. However, when the clay content becomes larger than 22 vol%, the increased viscosity and possible induced cohesive forces, exceed the lubricating effect, hence the velocity decreases (Fig. 9 E, F). Debris flows with a clay content of 22 vol% show an optimum in water turbulence and jumping particles, compared to flows with less or more clay. A clay cloud disperses in all direction, even if the debris flow stopped flowing (supporting movie S5 and S6). The results of this debris-flow behavior are clearly visible in the parabolic relation with wave celerity ($R^2 = 0.96$) and far-field wave amplitude ($R^2 = 0.79$), but are poorly reflected in the near-field wave amplitude (Fig. 10 E, F). In addition, the cloud of clay dispersing into the water body can locally increase the water density and might suppress the wave amplitude.

Supplementary data related to this article can be found at https://doi.org/10.1016/j.coastaleng.2019.103623.

Gravel content does not show any clear relation with the debris-flow thickness or velocity (Fig. 9 G, H), nonetheless when increasing the gravel content, a steeper wave front is observed. The impact of a debris flow with a higher gravel content leads to more turbulence in the water body; gravel is pushed upwards after impact, rises above the water level, and water droplets are ejected into the air (movie S7 in supporting information). Quantitatively, however, gravel content of the debris flow does not seem to have a strong relation with wave characteristics; an increase in gravel content leads to an increase in near-field crest amplitude ($R^2 = 0.50$), but in the far-field this relation is less significant.

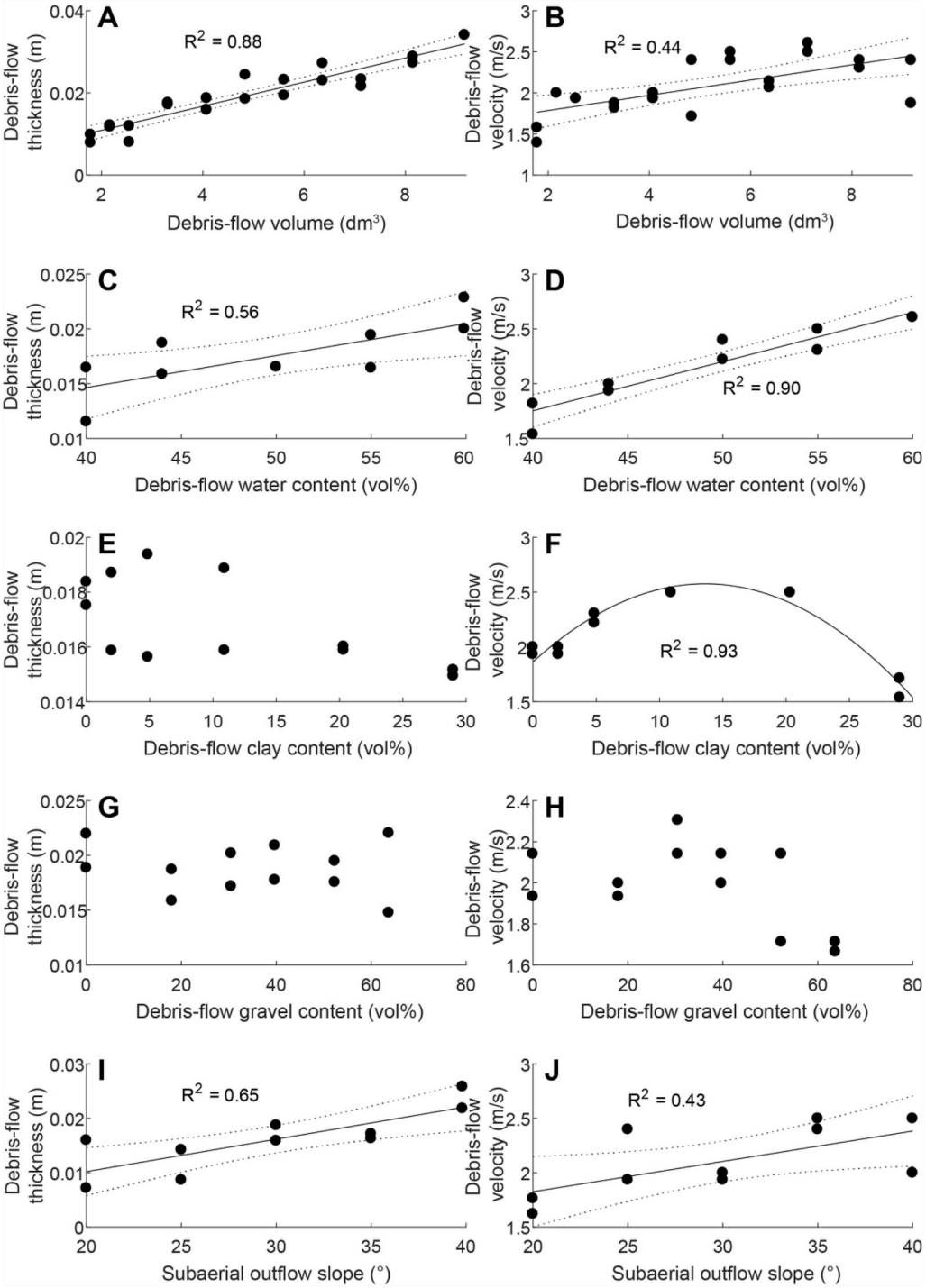

Fig. 9. Relation between initial debris-flow conditions and debris-flow characteristics and topography. The debris-flow thickness was measured at the channel outlet; debris-flow velocity is averaged over the whole subaerial outflow channel. Only relations with $R^2 > 0.4$ are shown, and all shown relations are significant ($p < 0.05$). The fitted curve in 9F is second-order polynomial, all other fits are linear; the corresponding parameters can be found in Table S2 in the supplementary materials. The dashed lines indicate the 95% confidence bounds for linear fits. Note the different y-axes.

Furthermore, there may be a decreasing celerity with increasing gravel content (Fig. 10 G, H).

Supplementary data related to this article can be found at https://doi.org/10.1016/j.coastaleng.2019.103623.

3.2.3. Outflow slope

Debris-flow velocity and thickness increase with increasing slope, but the relations are weak ($R^2 = 0.43$ and 0.65, respectively) (Fig. 9 I, J). With a low outlet slope of 20° the debris flow debouches smoothly into the water, and no impact crater or much turbulence occurs (movie S8 in supporting information). The wave detaches relatively quickly from the debris flow, and many small waves or ripples are formed. Increasing the slope leads to more turbulence, and water droplets are ejected into the air. Furthermore, a higher wave amplitude and wave celerity is observed (movie S9 in supporting information). The largest outflow slope we have used in our experiments (40°) results in less steep waves with a lower wave amplitude and celerity (Fig. 10 I, J).

Supplementary data related to this article can be found at https://doi.org/10.1016/j.coastaleng.2019.103623.

3.3. Influence of debris flow on tsunami

Here we explore to what extent debris-flow velocity, effective mass, energy and momentum control wave amplitude, wave celerity and

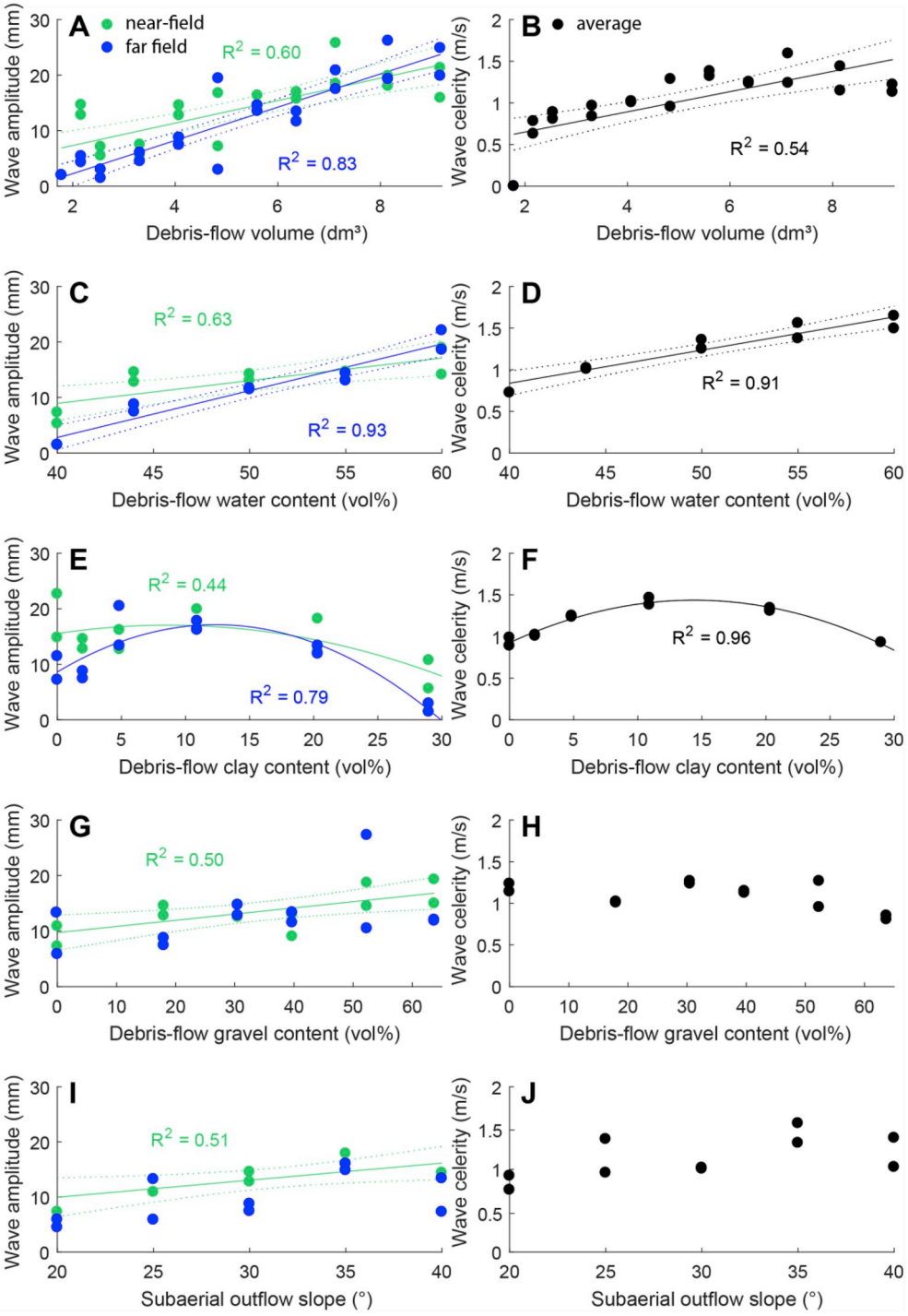

Fig. 10. Relation between initial debris-flow conditions and wave characteristics. The wave crest amplitude is the leading amplitude in the near-field (green, x = 0.50 m) and far-field (blue, x = 1.20 m). The wave celerity is averaged over the whole basin. Only relations with $R^2 > 0.4$ are shown, and all shown relations are significant ($p < 0.05$). The fitted curve in 10F is second-order polynomial, all other fits are linear; the corresponding parameters can be found in Table S2 in the supplementary materials. The dashed lines indicate the 95% confidence bounds for linear fits. (For interpretation of the references to color in this figure legend, the reader is referred to the Web version of this article.)

wavelength. These debris-flow parameters are influenced by debris-flow volume, composition and outflow slope (Figs. S2 and S3, in supporting information). Debris-flow velocity was averaged over the whole outflow slope; all other parameters were determined at the moment of impact using equations (1)–(3). All four parameters are positively correlated with the near and far-field wave amplitude, celerity and wavelength (Fig. 11).

There is a strong correlation between debris-flow velocity and wave celerity during wave generation ($R^2 = 0.79$), and the strength of this relation decreases with increasing distance from the impact zone (not shown). Effective mass shows the same correlation with wave characteristics as velocity, but the relations are weaker ($R^2 = 0.57$, 0.39 and 0.35 for far-field crest amplitude, wave celerity and wavelength, respectively).

Debris-flow energy and momentum are both calculated by using velocity and effective mass. An increase in debris-flow energy leads to an increase in maximum wave energy (assuming the wave is at its maximum at the moment of detachment; Fig. S4A). On average, the maximum wave energy is about 1–15% of the debris-flow energy, and the efficiency of energy transfer decreases with increasing debris-flow energy (Supporting Fig. S4B).

An increase in debris-flow energy leads to an increase in leading crest amplitude ($R^2 = 0.58$ in the far field), average crest celerity ($R^2 = 0.46$) and wavelength ($R^2 = 0.48$) (Fig. 11).

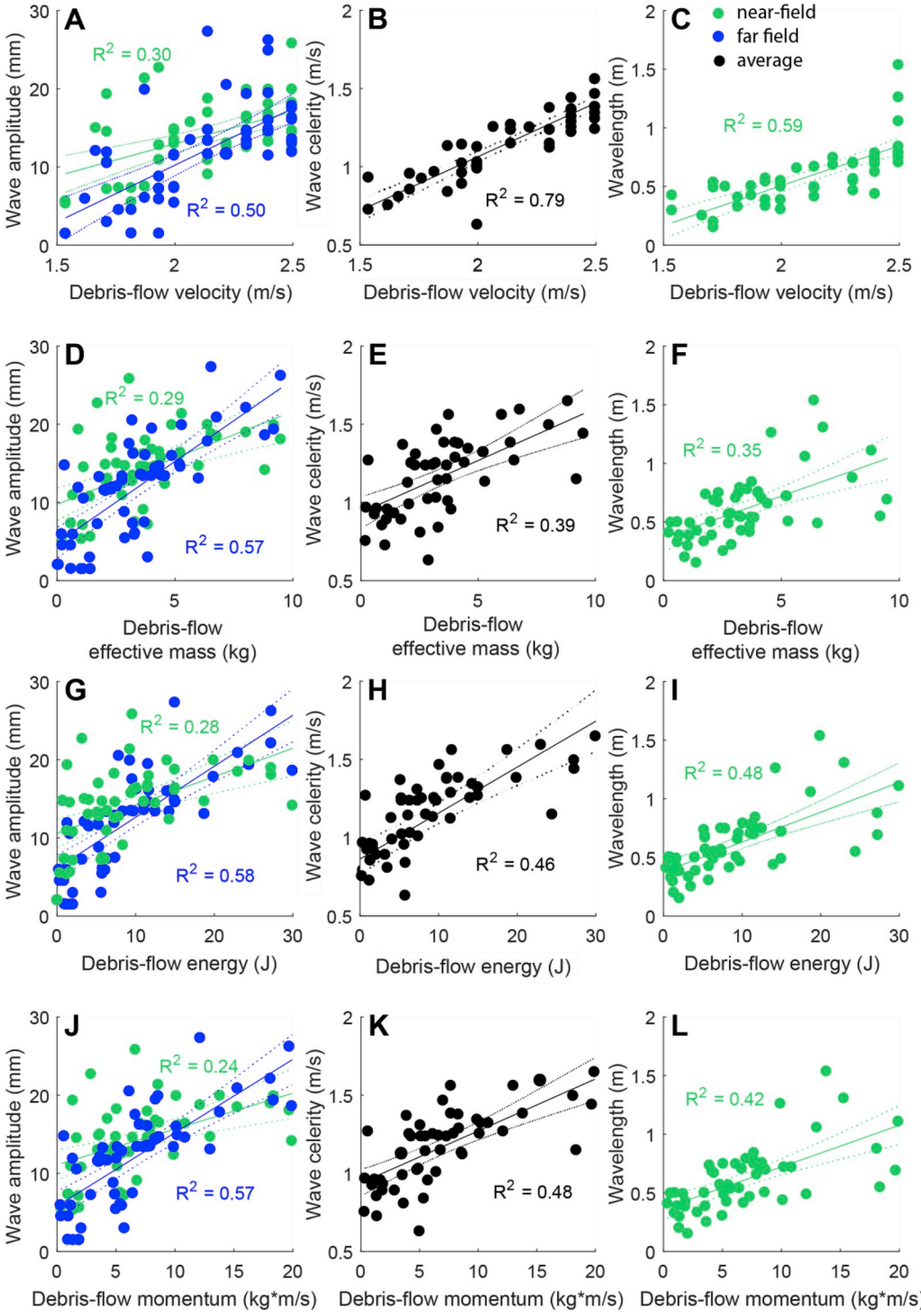

Fig. 11. Relation between debris-flow characteristics velocity, effective mass, energy and momentum; and wave characteristics leading wave crest amplitude in the near-field (x = 0.50 m, green) and far-field (x = 1.20m, blue), average crest celerity and near field wavelength (x = 0.50 m). The dashed lines indicate the 95% confidence bounds. All shown relations are significant ($p < 0.05$). The parameters corresponding to the shown linear fits can be found in Table S3 in the supplementary materials. (For interpretation of the references to color in this figure legend, the reader is referred to the Web version of this article.)

A higher momentum leads to a longer time until detachment, creates more powerful waves in terms of wavelength and crest amplitude (Fig. 11) and a larger near-field wave non-linearity (not shown). A lower momentum results in more and smaller waves, because the debris flow does not have enough momentum to keep pushing the waves for a long time and distance, and wave detachment occurs sooner. The relation with wave amplitude is strongest in the far field where the wave is fully developed and detached ($R^2 = 0.58$).

4. Discussion

In this section the results are interpreted and compared to literature (section 4.1), after which simple predictors and previously developed predictive equations will be assessed (section 4.2). Finally, the influence of scaling in this research is discussed (section 4.3).

4.1. The effects of debris-flow characteristics on tsunamis

We experimentally found that an increase in debris-flow volume leads to an increase in debris-flow thickness and velocity.

Correspondingly, the wave amplitude and celerity were increased. An increase in water content leads to a faster debris flow. Similar observations were obtained for an increase in clay content, until a certain threshold when the viscosity and cohesion of the flow became too large. The gravel content did not show a relation with the wave characteristics. The characteristics of the debris flow and waves were summarized in the parameters energy and momentum, which showed the same correlations with debris-flow volume, composition and outflow slope as the parameters they were derived from (debris-flow velocity and effective mass; see Figs. S1 and S2 in supporting information). Next, we will discuss our findings related to debris-flow and wave behavior and compare this to previously conducted research.

Our results regarding water and clay content of debris flows, follow the findings of de Haas et al. (2015), where water acts as a lubricant for the flow and an increase in clay content has the same effect, due to the better retained excess pore pressure (de Haas et al., 2015). In contrast to their research, there was no (parabolic) trend between gravel content and debris-flow or wave characteristics. They found that the runout length of the debris flow has an optimum at ~30 vol% gravel content. At a lower gravel content, the levees where insignificant, promoting lateral spread instead of longitudinal growth, while a large gravel content caused increased gravel accumulation at the flow front, reducing runout distance. The higher momentum of debris flows with higher percentage of courser particles, as found by McFall and Fritz (2016), was not observed.

Dimensionless parameter values of debris-flow and wave characteristics found in this research are remarkably similar compared to other studies and nature (Table 3). The relative wave period is somewhat lower, while the relative wave celerity is considerably larger. This indicates a relatively strong pushing effect of the debris flow, which might be related to the 10° slope of the wave basin and/or the higher mobility of a water saturated debris flow, causing a longer detachment time compared to studies with a horizontal basin slope and dry granular material.

After detachment, when the debris flow ceased to drive the wave, the wave slowed down and flattened out. A natural deep water tsunami travels with a constant wavelength and wave amplitude, and only starts to deform (decreasing wave period, increasing wave amplitude and increasing wave non-linearity) when approaching shallower water (Hammack, 1973). In deep water, the wave celerity is determined by the wave period, following the deep water equation ($c = gT/2\pi$). It is therefore expected that the celerity of the waves in this research will gradually recover from the oversteepening and acceleration caused by the imposed impulse, and will ultimately reach a constant wave period, wave celerity and wavelength if the reservoir would be long enough with extended flat bottom. Furthermore, the waves in this research were highly non-linear. A natural deep water tsunami travels as a dispersive, non-linear wave, where dispersion ($u^2 = h^2/\lambda^2$) and the non-linearity (here expressed as ε = wave height H/still water depth h) are in the same order of magnitude (Madsen et al., 2008). This is in agreement with the far-field waves in this research.

The Froude number (equation (7)), the ratio of landslide velocity to wave celerity, could give an indication for wave breaking behavior. In our research, no wave breaking occurred. Mulligan and Take (2017) state that for $Fr_{MT} > 1$ supercritical conditions occur, resulting in a breaking bore. When submerged, the debris flow slows down until $Fr_{MT} = 1$ where after the wave is released. For $Fr_{MT} < 1$, the debris flow still pushes the water, however the wave celerity exceeds the debris-flow velocity. This causes a non-breaking wave travelling away from its source region. Hence, at $Fr_{MT} = 1$, the largest wave amplitude can be formed.

The largest waves were indeed found in the detachment zone. However, in the current research, no breaking occurred although Fr_{MT} did exceed 1. This opposes the studies of Miller et al. (2017) or Heller and Hager (2010). Interestingly, $Fr_{MT} > 1$ was only satisfied for waves in the shallow part of the basin for which $a_c/h > 0.78$ (theoretical breaking limit; McCowan, 1894) was also true. This is again an indication that the waves in our experiment should break according to theory. The absence of breaking waves can likely be explained by the sloping bed of the wave basin. Waves which are about to break, travel to deeper water and therefore breaking does not occur for the range of parameters used in this study. Also the presence of suspended sediment (clay) can suppress the wave breaking behavior. Finally, suppression of wave breaking due to scaling effects could play a role, see section 4.3.2.

Wave amplitude, celerity and shape are evident in the wave energy. In the current study, 0.1–38% of the debris-flow energy was transferred to the waves (Fig. S4 in supporting information). This is in agreement with values found in previous studies (e.g. Mohammed and Fritz (2012) found 1–24%). Heller and Hager (2011) argued that energy transformation during impact is more efficient if the water splash is relatively

Table 3
Debris-flow and wave characteristics found in various comparable studies. Values are taken or calculated form the source in the header, unless specified otherwise in the footnotes. [a]calculation of relative values by using h = 0.165 m [b] calculation of relative values by using h = 20 m [c] Iverson (1997). [d] Hermanns et al. (2004). [e] Bussman and Anselmetti (2010). [f] Goff and Chauge-Goff (2014) [g] Mcfall and Fritz (2016). [h] if U > 1, the wave is non-linear (Lighthill, 2001).

		This study [a]	Fritz et al. (2004)	Heller and Hager (2010), 2011	Mohammed and Fritz (2012)	Heller and Spinneken (2015)	McFall and Fritz (2016)	Mulligan and Take (2017); Miller et al. (2017)	Natural debris flow and wave [b]
Debris-flow velocity [m/s]	u_s	1.00–3.74	–	2.06–8.77	–	0.94–3.79	–	2.5–4.8	0.01–1 [c]
Relative debris-flow height [−]	h_s/h	0.03–0.24	0.07–0.6	0.09–1.64	0.1–0.9	0.25–0.5	0.08–0.46	0.07–0.7	0.005–0.5 [c]
Relative wave amplitude [−]	a_c/h	0.01–0.2	0.05–1.3	<2.5	<0.38	0.003–1.23	0.001–0.35	0.2–2.5	1–10 [d e]
Relative wave celerity [−]	$c\sqrt{gh}$	4.9–12.7	0.3–2.5	–	0.7–1.2	~0.5–1.5	0.70–1.3	4.0–11.5	<~19 [f]
Relative wave period [−]	$T\sqrt{g/h}$	3.62–7.9	6–22	~1–40	6–26	6.1–31.3	2–22	–	~2.6 [f]
Froude number [−]	$u_s/\sqrt{gh}$	1.4–2.6	~1.0–4.8	0.9–6.8	1–4	0.5–2.5	1.0–3.9	~0.2–4.8 [a]	1–4 [g]
Ursell number [-][h]	$a_c\,\lambda^2/h^3$	0.01–95	1–22	2.7–10^4	0.2–55	0.5–10^3	0.01–55	–	–

small and limited air is entrained, which is true for flows with a relatively low debris-flow energy, which is also found in this study. Furthermore, the impact with the channel bottom played a role in their research, but this is negligible in this study due to the sloping bottom. Presumably only at an outflow slope of 40°, the difference between the outflow slope and the wave basin became so large that most of the energy was lost by impact during the transition from outflow slope to wave basin. The lower energetic waves formed at the highest outflows slope angle, could be the result of this phenomenon.

4.2. Prediction of wave characteristics

4.2.1. Prediction of near-field wave characteristics with basic debris-flow parameters

In this section, relative debris-flow parameters that are straightforward to measure are related to wave characteristics (Table 4), to explore the possibility of predictive relations for provide quick estimations of wave characteristics required for hazard management. Most relations are relatively strong ($R^2 > 0.5$) for at least one debris-flow parameter. Wave celerity, wavelength, far-field crest amplitude and wave energy are clearly a function of debris-flow characteristics. However, near-field leading crest amplitude, maximum crest amplitude and detachment time are not fully related to any of the debris-flow features.

Wave celerity and wavelength turn out to be the best related to debris-flow velocity. Average wave celerity was approximately 0.5 times the average debris-flow velocity during outflow. This allowed the water to be pushed up by the debris flow, which took much less time than the time to wave detachment. The larger the difference between the velocity and celerity, the more the water will be pushed up before wave release. The strength of the relation between debris-flow velocity and wave celerity decreases with increasing distance from the impact area, indicating that the debris-flow velocity largely determines the near-field wave celerity and potentially showing the impact of the sloping bed. As shown in section 3.2, debris-flow velocity mostly depends on water and clay content, which both can be a lubricant for the flow. It is therefore an important conclusion to state that debris-flow composition does matter for tsunami assessment.

Momentum was found to be the most important characteristic for wave amplitude prediction by Mulligan and Take (2017) and Bullard et al. (2019), which matches the findings in this research. The majority of the momentum and debris-flow energy are transferred almost instantly at the impact (Heller et al., 2016). Secondary waves are formed if the momentum transfer of the debris flow to the water is not large enough to oppose the restoring force due to the upstream pressure gradient of water. Debris flows with a small momentum will therefore result in multiple smaller waves, while larger momentum flows will generate one larger wave. Both debris-flow energy and momentum can indeed be related to the wave characteristics. Both parameters are a measure of debris-flow effective mass and velocity, but their combined effect is not always better than assessing the debris-flow velocity only, however.

Effective mass, energy and momentum are variables which are not only dependent on the debris-flow characteristics, but also on the wave generation and development, since the detachment time partly determines the effective mass. They are therefore less suitable variables for potential wave characteristic predictors, and there is the need to find a way to estimate detachment time.

The strength of the relations between debris-flow and tsunami characteristics can give an indication to which extend debris-flow variables can be used for prediction of wave properties. The obtained relations are relatively strong, even in our experimental settings where we created a lot of variability by using different types of debris flows. Therefore, debris-flow velocity and momentum are good predictors for wave celerity and far-field leading wave amplitude, respectively.

4.2.2. Applicability of maximum crest amplitude predictors to debris-flow generated tsunamis

In section 4.2.1 we focused on predicting the leading crest amplitude and wave celerity by using relatively simple parameters. Leading crest amplitude and wave celerity are both of crucial importance for hazard management; and simple debris-flow parameters can be a quick and easy way for hazard assessment.

The previously developed wave amplitude predictors as described in section 2.5 are all developed for predicting maximum near-field wave crest amplitude, generated by landslides with idealized initial and boundary conditions. Those predictors are aiming on predicting the maximum crest amplitude instead of the leading crest amplitude as dealt with in section 4.2.1, which is poorly predicted by our simple parameters (Table 4). Therefore, the applicability of the previously developed equations needs to be assessed for a wide range of debris flows with strongly varying dynamics. One should note that the crest amplitude is measured at the side of the wave basin as described in section 2.2 and that this approach differs from the studies discussed below.

All near-field wave crest amplitude equations assume a horizontal

Table 4
R^2 values (indicating a significant ($p < 0.05$) linear correlation) of debris-flow characteristics and the corresponding wave characteristics. The darker the green color, the stronger the correlation. FZ04 refers to the research of *Fritz et al. (2004)*, HH10 to *Heller and Hager (2010)*, MT17 to *Mulligan and Take (2017)* and BL19 to *Bullard et al. (2019)*. *) the strength of the relation depends on the water depth used in equations (13) and (14), see Fig. 12.

variables	R^2-value in experimental results				FZ04	HH10	MT17	BL19
Debris flow → Waves ↓	*velocity* u_{df}	*effective mass* m_{eff} *(eq2)*	*energy* E_{df} *(eq3)*	*momentum* M *(eq1)*	*eq5*	*eq9, 10*	*eq13*	*eq14*
Maximum crest amplitude	0.33	0.35	0.30	0.33	0.41	0.54	0.54-0.57*	0.54-0.57*
Near-field leading crest amplitude (x = 0.50 m)	0.30	0.29	0.28	0.24				
Far-field leading crest amplitude (x = 1.20 m)	0.50	0.57	0.57	0.58				
Average crest celerity	0.79	0.39	0.46	0.48				
Near-field wavelength (x = 0.50 m)	0.59	0.35	0.48	0.42				
Near-field wave energy (x = 0.50 m)	0.53	0.53	0.68	0.64				
Detachment time	0.30	0.50	0.40	0.47				

wave basin bed, while our sloping bed results in a gradually increasing water depth. To find the most suitable depth, all calculations are performed with three water depths: in the near field (x = 0.5 m, h = 0.079 m), around the detachment zone (x = 0.8 m, h = 0.123 m) and in the far field, the maximum water depth (x = 2.0 m, h = 0.33 m).

The predictors are developed for near-field predictions. Their predictive capacity for maximum crest amplitude occurring at different locations, is indeed the strongest when the maximum amplitude occurs in the near-field region before detachment (x < 0.85 m). Furthermore, the predictors are used for predicting wave amplitude in shallow water depths, outside of their range of applicability. It is therefore possible that surface tension or density effects from the suspended sediment, can influence the strength of the relation. See section 4.3 for a more detailed discussion about scaling.

The predictor of Fritz et al. (2004) (Fig. 12 A, B, C; equation (5)) structurally under predicts the wave amplitude, and cannot be improved by adapting the water depth. The choice of the water level does not influence the strength of the predictor, but it slightly changes the RMSE (root mean square error; ranging from 13.82 to 14.22 mm). The under prediction could possibly be explained by the wave basin slope of 10°, which could lead to a longer detachment time and thus a larger momentum transfer, hence a different wave behavior than predicted with this semi-empirical equation.

The predictor of Heller and Hager (2010) (Fig. 12 D, E, F; equations (9) and (10)) which is also based on the Froude number, captures the general amplitude trend much better (RMSE 5.29–7.99 mm, $R^2 = 0.54$). The applicability of the equation of Mulligan and Take (2017) (equation (13)) strongly depends on water depth (Fig. 12 G, H, I). When predicting wave amplitude with the water depth in the near field or at the detachment location, it strongly overestimates wave amplitude (RMSE = 28.52–42.97 mm). Possible explanation for the over estimation can be the 3D character of our study and the down-sloping bed. Using the

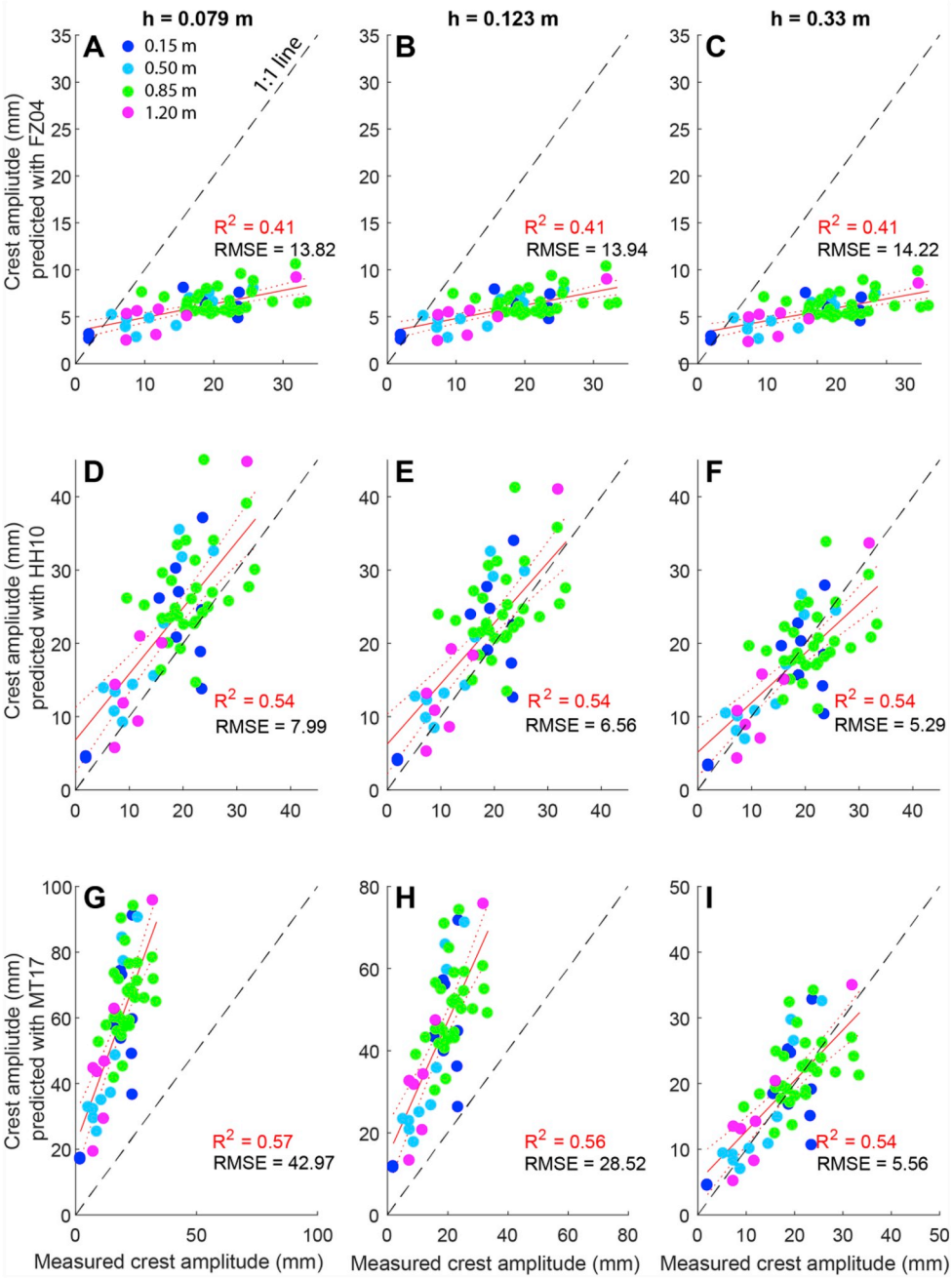

Fig. 12. Prediction of maximum wave crest amplitude against measured maximum wave crest amplitude, for three different water depths (h = 0.079, 0.123 and 0.33 m) and three different predictors. The measured amplitude is the largest amplitude measured at any time at any location during the experimental run, and the location at which this occur is indicated by a color. FZ04 refers to equation (5) (Fritz et al., 2004), HH10 refers to equations (9) and (10) (Heller and Hager, 2010) and MT17 to equation (13) (Mulligan and Take, 2017). R^2 values indicate how well the two datasets are correlated, indicated by the red line, with the red-dashed lines being the 95% confidence bounds of the linear regression. RMSE indicates the root mean square error. (For interpretation of the references to color in this figure legend, the reader is referred to the Web version of this article.)

maximum water depth of our setup, h = 0.33 m, the predicted and measured crest amplitude coincide relatively well (RMSE = 5.56 mm), but the correlation is less strong (R^2 = 0.54 instead of 0.57 at h = 0.079 m). Applying the equation of Bullard et al. (2019) to our data (not shown), yields the same problems as the equation of Mulligan and Take (2017), however the wave amplitude is even more over-estimated (R^2 = 0.57, 0.56 and 0.54; RMSE = 84.06, 64.16 and 21.59 mm; for h = 0.079, 0.123, 0.33 m respectively).

The predictors of Heller and Hager (2010) and Mulligan and Take (2017) give, despite their very different character, similar results for h = 0.33 m, which was also noticed by Mulligan and Take (2017). The relatively large correlation coefficients are promising, but adjustments have to be made to improve the 1:1 fit. It shows that the assumption of momentum exchange is also valid for saturated debris flows, following Bullard et al. (2019). However, the correct fit results from using the maximum water depth, which indicates that future work to further elucidate the effect of a sloping wave basin floor is warranted.

In short, near-field wave celerity is best predicted by using the debris-flow velocity. Prediction of wave amplitude is more challenging, and the maximum amplitude is most accurately assessed by using the momentum-based equation of Mulligan and Take (2017), although a sloping wave basin should be incorporated in the equation. The amplitude of the far-field leading crest is also highly important for hazard mitigation, and its prediction by using debris-flow momentum gives reasonable results. Prediction of the near-field leading crest amplitude remains challenging.

4.3. Scaling

Following Hooke and Rohrer (1979) and Paola et al. (2009), small scale laboratory experiments can provide important information about the understanding of debris flows and can provide quantitative results (Kleinhans et al., 2014). Below we zoom in on debris-flow and wave scaling.

4.3.1. Debris-flow scaling

Debris-flow and wave behavior in this setup are comparable to larger-scale studies. In earlier subaerial research with the same setup, de Haas et al. (2015) found a flow behavior, deposit morphology, grain size sorting, channel width-depth ratio, and a runout length comparable to nature. Therefore, relations found in this research are likely applicable to natural situations, although the quantitative correlations may not be directly applicable to the field scale.

Potential scale dependent behavior is assessed by comparing a range of (non)dimensional parameters of this study to the large scale experimental research of Iverson (1997) and natural debris flows (Table 5 and Table S4 in supporting information). A small setup means a relatively large influence of flow viscosity, capillary forces and grain inertia, but a disproportionally small influence of pore pressure on the debris-flow behavior (Iverson, 1997; Iverson et al., 2010). This results in a large Bagnold number (large influence of collisional forces of grains) and a large particle Reynolds number (larger effect of particle collision than pore fluid viscosity). These scaling issues could affect the thickness and velocity of the debris flow, and therefore the generated tsunami. However, there is no indication that this would substantially affect the relations found in this research.

4.3.2. Wave scaling

Despite the small experimental setup in this research, dimensionless parameter values and wave characteristics found in this research are remarkably similar compared to other studies and nature (Table 3). When assessing the traditional scaling rules as described in Heller (2011), the Reynolds (*Re*) and Froude (*Fr*) number fall within the range of the rule of thumb determined by Heller et al. (2008) for impulse transfer. However, with the average water depth used in this setup, scale effects for surface tension should be considered. Heller (2011) states that surface tension becomes relevant in models which include wave breaking (air entrainment), small water depths and capillary waves. Surface tension could suppress the wave height and increase dissipation. However, the suppression of wave height in combination with the surface tension, could also hinder breaking, resulting in a larger wave amplitude than when breaking would have occurred.

To determine the influence of scale effects on waves, the Weber number (W_b) is calculated (equation (S11) in supporting Table S4). In this research, $W_b > 60$ indicates that inertial forces are dominant over surface tension forces. To avoid the dominance of scale effects, runs with capillary waves (<2 mm) are neglected, which was only necessary at a few low volume runs and very far-field waves.

The capillary force acting on one wave, expressed in surface tension energy (surface tension coefficient for water, 0.07 N/m times surface area of the wave), is < 0.005 J. On average, the surface tension is about 1% of the size of the wave energy, which is at the limit of the traditional scaling rules (Hughes, 1993). This amount is negligible considering qualitative relations, although this implies that quantitative relations found cannot be used directly in the field. It might also affect the quality of the fit of the wave amplitude predictors discussed in section 4.2 (Miller et al., 2017).

Table 5
(non)Dimensional parameters of this small scale study compared to the USGS flume and natural debris flows, modified from de Haas et al. (2015). Values are taken or calculated form the source specified in the header unless specified otherwise in the footnotes. [a] Iverson (1997). [b] de Haas et al. (2015). [c] Major (2000). [d] Iverson et al. (2010). [e] Iverson and Denlinger (2001). [f] Zhou and Ng (2010). [g] Estimated values.

Parameter	Symbol (unit)	This study	Natural debris flows[a]	USGS Flume[a]
Grain diameter	δ (m)	0.0005–0.003	10^{-5} - 10^{1}	0.001
Flow thickness	h_s (m)	0.005–0.04	0.1–10	0.1
Flow velocity	u_s (m/s)	1.00–3.74	0.1–20	10
Flow shear rate	γ (1/s)	44.5–300.8	1–100	100
Solid density	ρ_s (kg/m^3)	2 650–3 400	2 500–3 000	2 700
Fluid density	ρ_w (kg/m^3)	1 000	1 000–1 200	1 100
Solid volume fraction	v_s (−)	0.4–0.6	0.4–0.8	0.6
Fluid volume fraction	v_f (−)	0.4–0.6	0.2–0.6	0.4
Fluid viscosity	μ (Pa s)	0.001–0.0035[b]	0.001–0.1	0.001
Friction angle	ϕ (°)	42[g]	25–45	40
Hydraulic permeability	k (m^2)	1.1×10^{-16}–2.1×10^{-13} [b]	10^{-13}–10^{-9}	10^{-11}
Hydraulic diffusivity	D (m^2/s)	5.8×10^{-9}–1.2×10^{-1} [b]	10^{-8} - 10^{-2} [c]	10^{-4} [c]
Slide Froude number	Fr (−)	2.9–7.7	0.01–20.2	10.1
Savage number	Sv (−)	3.51×10^{-5} - 0.49	10^{-7} - 10^{0} [a, e, f]	0.2
Bagnold number	Bg (−)	1.12×10^{4} - 3.59×10^{6}	10^{0} - 10^{8} [a, e]	400
Friction number	Fn (−)	117–5.25×10^{4}	10^{0} - 10^{5} [a, f]	$2*10^{3}$
Mass number	Mn (−)	1.8–4.0	1–10 [b]	4
Darcy number	Dc (−)	7.75×10^{3} - 6.74×10^{8}	10^{4}–10^{8}	600
Reynolds number	Re (−)	4.33×10^{4} - 1.04×10^{5}	10^{5}–10^{7} [d, e]	$3*10^{3}$ [d]
Particle Reynolds number	Re_g (−)	2.82×10^{3} - 2.03×10^{6}	0.01–2 [a, f]	100

5. Conclusions

Debris-flow generated tsunamis are particularly dangerous because of their unpredictability and large and fast waves, which can have devastating effects on landscape and society. This study aims to unravel the influence of debris-flow volume, debris-flow composition and

subaerial slope on wave characteristics, and to test suitable predictors for wave celerity and amplitude. A total of 60 experiments were conducted within a small scale 2D-3D physical laboratory model, in which the total source volume of the debris flow (1.8–9.2 dm^3), water content (40–60 vol%), gravel content (0–64 vol%), clay content (0–29 vol%) and outflow slope (20–40°) are systematically varied. The herein presented results of the experimental study can be summarized as followed:

- Upon debouching in the reservoir, the debris flow pushes the water forward, transferring 0.1–38% of its energy to the leading crest, hereby oversteepening and accelerating the wave. The wave is detached when the wave celerity exceeds the debris-flow velocity. Debris flows with a low momentum and energy result in a relatively small amount of air entrainment during wave generation, a quick release of the wave and therefore the development of more, smaller waves following the leading crest.
- Wave amplitudes are the largest (up to 34 mm) just after detachment, at a distance of 0.50–0.85 m from the channel outlet. Wave celerity (0.62–1.65 m/s) increases by the pushing of the debris flow, and decreases after detachment with increasing travel distance and therefore increasing water depth, towards the value predicted by the deep water approximation. The wave period (0.47–1.03 s) increases in the far-field. Both are the result of the oversteepening and acceleration caused by the pushing of the debris flow in the near-field zone.
- Debris-flow thickness is mostly determined by its volume, while velocity is mostly controlled by water and clay content due to their lubricating effect. The trends in debris-flow thickness and velocity are reflected in the wave amplitude and celerity of the leading waves.
- Debris-flow velocity is the best predictor for wave celerity and wavelength. The far-field amplitude of the leading crest shows a relatively weak correlation to debris-flow characteristics, but is best estimated using debris-flow momentum.
- Near-field maximum crest amplitude predictors that were previously found to be applicable to dry-landslide generated tsunamis, can also be used to predict waves generated by a wide range of debris flows. The equations perform reasonably well with our experimental data, despite the assumptions made regarding water depth. The wave amplitude predictor of Fritz et al. (2004) underestimates the measured maximum wave amplitude, while Heller and Hager's (2010) Froude-number based equation works relatively well. The wave amplitude predictor of Mulligan and Take (2017) is highly sensitive to water depth, and performs the best using the maximum water depth in our setting. It shows that the assumption of momentum exchange, contrary to Mulligan and Take's (2017) constraints and following Bullard et al. (2019), is also valid for saturated (highly mobile) debris flows.

Declaration of competing interest

The authors declare that they have no known competing financial interests or personal relationships that could have appeared to influence the work reported in this paper.

CRediT authorship contribution statement

S.I. de Lange: Investigation, Formal analysis, Visualization, Writing - original draft, Writing - review & editing. **N. Santa:** Investigation. **S.P. Pudasaini:** Conceptualization, Funding acquisition. **M.G. Kleinhans:** Supervision. **T. de Haas:** Conceptualization, Methodology, Supervision, Funding acquisition.

Acknowledgments

We thank R. Mulligan and two anonymous reviewers for their constructive and helpful comments and suggestions. This paper was written by SdL on the basis of her MSc thesis supervised by TdH. This research has been financially supported by the German Research Foundation (DFG), project Nr. PU 386/5–1: "A novel and unified solution to multi-phase mass flows: U_MultiSol" granted to SP and TdH. Supplementary Table S1 summarizes all data, and example movies are given in supplementary movies S1-S9. All analyzed movies are available upon request for more detailed analysis.

Appendix A. Supplementary data

Supplementary data to this article can be found online at https://doi.org/10.1016/j.coastaleng.2019.103623.

References

Ataie-Ashtiani, B., Nik-Khah, A., 2008. Impulsive waves caused by subaerial landslides. Environ. Fluid Mech. 8, 263–280.
Atwater, B.F., Moore, A.L., 1992. A tsunami about 1000 Years ago in puget sound, Washington. Science, New Series 258 (5088), 1614–1617.
Bullard, G.K., Mulligan, R.P., Carreira, A., Take, W.A., 2019. Experimental analysis of tsunamis generated by the impact of landslides with high mobility. Coast Eng. 103538.
Bussmann, F., Anselmetti, F.S., 2010. Rossberg landslide history and flood chronology as recorded in Lake Lauerz sediments (Central Switzerland). Swiss J. Geosci. 103, 43. https://doi.org/10.1007/s00015-010-0001-9.
D'Agostino, V., Cesca, M., Marchi, L., 2010. Field and laboratory investigations of runout distances of debris flows in the Dolomites (Eastern Italian Alps). Geomorphology 115 (3–4), 294–304.
Dawson, A.G., Stewart, I., 2007. Tsunami deposits in the geological record. Sediment. Geol. 200 (3–4), 166–183.
de Haas, T., Braat, L., Leuven, J.R.F.W., Lokhorst, I.R., Kleinhans, M.G., 2015. Effects of debris flow composition on runout, depositional mechanisms, and deposit morphology in laboratory experiments. J. Geophys. Res. Earth Surf. 120.
de Haas, T., van den Berg, W., Braat, L., Kleinhans, M.G., 2016. Autogenic avulsion, channelization and backfilling dynamics of debris-flow fans. Sedimentology 63 (6), 1596–1619.
de Haas, T., Kruijt, A., Densmore, A.L., 2018. Effects of debris-flow magnitude–frequency distribution on avulsions and fan development. Earth Surf. Process. Landforms 43 (13), 2779–2793.
Fritz, H.M., Hager, W.H., Minor, H.E., 2004. Near field characteristics of landslide generated impulse waves. J. Waterw. Port, Coast. Ocean Eng. 130 (6), 287–302.
de Haas, T.D., van Woerkom, T.V., 2016. Bed scour by debris flows: experimental investigation of effects of debris-flow composition. Earth Surf. Process. Landforms 41 (13), 1951–1966.
Fritz, H.M., Hager, W.H., Minor, H.E., 2003a. Landslide generated impulse waves. 1. Instantaneous flow fields. Exp. Fluid 35, 505–519.
Fritz, H.M., Hager, W.H., Minor, H.E., 2003b. Landslide generated impulse waves. 2. Hydrodynamic impact craters. Exp. Fluid 35, 520–532.
Goff, J., Chauge-Goff, C., 2014. The Australian tsunami database: a review. Prog. Phys. Geogr. 38 (2), 218–240.
Hammack, J.L., 1973. A note on tsunamis: their generation and propagation in an ocean of uniform depth. J. Fluid Mech. 60 (4), 769–799.
Heidarzadeh, M., Muhari, A., Wijanarto, A.B., 2019. Insights on the source of the 28 september 2018 sulawesi tsunami, Indonesia based on spectral analyses and numerical simulations. Pure Appl. Geophys. 176, 25.
Heller, V., 2011. Scale effects in physical hydraulic engineering models. J. Hydraul. Res. 49 (3), 293–306.
Heller, V., Hager, V.H., Minor, H.E., 2008. Scale effects in subaerial landslide generated impulse waves. Exp. Fluid 44 (5), 691–703.
Heller, V., Hager, V.H., Minor, H.E., 2009. Landslide generated impulse waves in reservoirs – basics and computation. In: Boes, R. (Ed.), VAW-mitteilung, vol. 211. ETH Zurich, Zurich.
Heller, V., Hager, W.H., 2010. Impulse product parameter in landslide generated impulse waves. J. Waterw. Port, Coast. Ocean Eng. 136 (3), 145–155.
Heller, V., Hager, W.H., 2011. Wave types of landslide generated impulse waves. Ocean. Eng. 38 (4), 630–640.
Heller, V., Spinneken, J., 2015. On the effect of the water body geometry on landslide–tsunamis: physical insight from laboratory tests and 2D to 3D wave parameter transformation. Coast Eng. 104, 113–134.
Heller, V., Bruggemann, M., Spinneken, J., Rogers, B.D., 2016. Composite modelling of subaerial landslide tsunamis in different water body geometries and novel insight into slide and wave kinematics. Coast. Eng. 109, 20–41.
Hermanns, R.L., Niedermann, S., Ivy-Ochs, S., Kubik, P.W., 2004. Rock avalanching into a landslide-dammed lake causing multiple dam failure in Las Conchas valley (NW Argentina) — evidence from surface exposure dating and stratigraphic analyses. Landslides 1, 113–122.
Higman, B., Shugar, D.H., Stark, C.P., Ekström, G., Koppes, M.N., Lynett, P., et al., 2018. The 2015 landslide and tsunami in Taan Fiord, Alaska. Sci. Rep. 8, 12993.
Hooke, R.B., Rohrer, W.L., 1979. Geometry of alluvial fans: effect of discharge and sediment size. Earth Surf. Process. 4, 147–166.
Huber, A., 1980. Schwallwellen in Seen als Folge von Bergstürzen, VAW Mitteil. 47, Versuchsanst. Für Wasserbau, Hydrol. und Glaziol. ETH Zurich, Zurich, Switzerland.

Hughes, S.A., 1993. Advanced Series on Ocean Engineering 7. Physical Models and Laboratory Techniques in Coastal Engineering. World Scientific, London.
Hürlimann, M., McArdell, B.W., Rickli, C., 2015. Field and laboratory analysis of the runout characteristics of hillslope debris flows in Switzerland. Geomorphology 232, 20–32.
Ilstad, T., Elverhøi, A., Issler, D., Marr, J.G., 2004b. Subaqueous debris flow behaviour and its dependence on the sand/clay ratio: a laboratory study using particle tracking. Mar. Geol. 213 (1–4), 415–438.
Iverson, R.M., 1997. The physicis of debris flows. Rev. Geophys. 35 (3), 245–296.
Iverson, R.M., Denlinge, R.P., 2001. Flow of variably fluidized granular masses across three-dimensional terrain: 1. Coulomb mixture theory. J. Geophys. Res. 106 (B1), 537–552.
Iverson, R.M., Logan, M., LaHusen, R.G., Berti, M., 2010. The perfect debris flow? Aggregated results from 28 large-scale experiments. J. Geophys. Res. 115, F03005.
Kafle, J., Pokhrel, P.R., Khattri, K.B., Kattel, P., Tuladhar, B.M., Pudasaini, S.P., 2016. Landslide-generated tsunami and particle transport in mountain lakes and reservoirs. Ann. Glaciol. 57 (71).
Johnson, A.M., 1970. Physical Processes in Geology. Freeman and Cooper, San Francisco, California.
Kafle, J., Kattel, P., Mergili, M., Fischer, J.-T., Pudasaini, S.P., 2019. Dynamic response of submarine obstacles to two-phase landslide and tsunami impact on reservoir. Acta Mech. 230, 3143–3169.
Kleinhans, M.G., van Dijk, W.M., van de Lageweg, W.I., Hoyal, D.C.J.D., van Maarseveen, M., Roosendaal, C., van Weesep, W., van Breemen, D., Hoendervoogt, R., Cheshier, N., 2014. Quantifiable effectiveness of experimental scaling of river- and delta morphodynamics and stratigraphy. Earth Sci. Rev. 133, 43–61.
Lamb, H., 1932. Hydrodynamics. Dover, New York, NY.
Legros, F., 2002. The mobility of long-runout landslides. Eng. Geol. 63 (3–4), 301–331.
Lighthill, J., 2001. Waves in Fluids. Cambridge University Press, Cambridge, UK.
Ma, G., Kirby, J.T., Hsu, T., Shi, F., 2015. A two-layer granular landslide model for tsunami wave generation: theory and computation. Ocean Model. 93, 40–55.
Madsen, P.A., Fuhrman, D.R., Schaffer, H.A., 2008. On the solitary wave paradigm for tsunamis. J. Geophys. Res. 113, C12012.
Major, J.J., 2000. Gravity-driven consolidation of granular slurries—implications for debris-flow deposition and deposit characteristics. J. Sediment. Res. 70 (1), 64–83.
McCowan, J., 1894. On the highest wave of permanent type. Philos. Mag. 38 (233), 351–358.
McFall, B.C., Fritz, H.M., 2016. Physical modelling of tsunamis generated by 3D deformable granular landslides on planar and conical island slopes. Proc. R. Soc. A 472 (2188), 20160052.
McFall, B.C., Mohammed, F., Fritz, H.M., Liu, Y., 2018. Laboratory experiments on three-dimensional deformable granular landslides on planar and conical slopes. Landslides 15, 1713–1730.
Mergili, M., Fischer, J.T., Krenn, J., Pudasaini, S.P., 2017. r.avaflow v1, an advanced open-source computational framework for the propagation and interaction of two-phase mass flow. Geosci. Model Dev. (GMD) 10, 553–569.
Mergili, M., Emmer, A., Juricova, A., Cochachin, A., Fischer, J.T., Huggel, C., Pudasaini, S.P., 2018a. How well can we simulate complex hydro-geomorphic process chains? The 2012 multi-lake outburst flood in the santa cruz valley (Cordillera Blanca, Peru). Earth Surf. Process. Landforms 43, 1373–1389.
Mergili, M., Frank, B., Fischer, J.T., Huggel, C., Pudasaini, S.P., 2018b. Computational experiments on the 1962 and 1970 landslide events at Huascaran (Peru) with r.avaflow: lessons learned for predictive mass flow simulations. Geomorphology 322, 15–28.
Miller, G.S., Take, W.A., Mulligan, R.P., McDougall, S., 2017. Tsunamis generated by long and thin granular landslides in a large flume. J. Geophys. Res. Oceans 122.
Mohammed, F., Fritz, H.M., 2012. Physical modelling of tsunamis generated by three-dimensional deformable granular landslides. J. Geophys. Res. 117, C11015.
Mulligan, R.P., Take, W.A., 2017. On the transfer of momentum from a granular landslide to a water wave. Coast Eng. 125, 16–22, 2017.
Najafi-Jilani, A., Ataie-Ashtiani, B., 2008. Estimation of near-field characteristics of tsunami generation by submarine landslide. Ocean. Eng. 35, 545–557, 2008.
Noda, E., 1970. Water waves generated by landslides. J. Waterw. Port, Coast. Ocean Eng. 96 (4), 835–855.
Panizzo, A., DeGirolamo, P., Petaccia, A., 2005. Forecasting impulse waves generated by subaerial landslides. J. Geophys. Res. 110, C12025.
Paola, C., Straub, K., Mohrig, D., Reinhardt, L., 2009. The "unreasonable effectiveness" of stratigraphic and geomorphic experiments. Earth Sci. Rev. 97, 1–43.
Pudasaini, S.P., 2012. A general two-phase debris flow model. J. Geophys. Res. 117. F03010, 1-28.
Pudasaini, S.P., 2014. Dynamics of submarine debris flow and tsunami. Acta Mech. 225, 2423–2434.
Pudasaini, S.P., Miller, S.A., 2013. The hypermobility of huge landslides and avalanches. Eng. Geol. 157, 124–132.
Pudasaini, S.P., Mergili, M., 2019. A multi-phase mass flow model. Journal of Geophysical Research – Earth Surface. https://doi.org/10.1029/2019JF005204.
Quecedo, M., Pastor, M., Herreros, M.I., 2004. Numerical modelling of impulse wave generated by fast landslides. Int. J. Numer. Methods Eng. 59 (12), 1633–1656.
Saelevik, G., Jensen, A., Pedersen, G., 2009. Experimental investigation of impact generated tsunami; related to a potential rock slide, Western Norway. Coast. Eng. 56, 897–906.
Scheidl, C., McArdell, B.W., Rickenmann, D., 2014. Debris-flow velocities and superelevation in a curved laboratory channel. Can. Geotech. J. 52 (3), 305–317.
Van Rijn, L.C., Tonnon, P.K., Sánchez-Arcilla, A., Cáceres, I., Grüne, J., 2011. Scaling laws for beach and dune erosion processes. Coast Eng. 58 (7), 623–636.
Walder, J.S., Watts, P., Waythomas, C.F., 2006. Case study: mapping tsunami hazards associated with debris flow into a reservoir. J. Hydraul. Eng. 132, 1.
Wang, F.W., Zhang, Y.M., Huo, Z.T., Matsumoto, T., Huang, B.L., 2004. The july 14, 2003 qianjiangping landslide, three Gorges reservoir, China. Landslides 1, 157–162. https://doi.org/10.1007/s10346-004-0020-6.
Watts, P., Walder, J.S., 2003. Evaluating tsunami hazards from debris flows. In: Paper to Be Presented at the 3rd International Conference on Debris-Flow Hazards Mitigation. Swiss Fed. Inst. for., Snow and Landscape Res, Davos, Switzerland, 10–12 Sept.
Yin, M., Rui, Y., 2018. Laboratory study on submarine debris flow. Mar. Georesour. Geotechnol. 36 (8), 950–958.
Zhou, G.G.D., Ng, C.W.W., 2010. Dimensional analysis of natural debris flows. Can. Geotech. J. 47 (7), 719–729.
Zweifel, A., Zuccalà, D., Gatti, D., 2007. Comparison between computed and experimentally generated impulse waves. J. Hydraul. Eng. 133, 2.